Human iPSC-derived neurons reveal early developmental alteration of neurite outgrowth in the late-occurring neurodegenerative Wolfram syndrome

Sandra Pourtoy-Brasselet,[3,6] Axel Sciauvaud,[1,2,6] Maria-Gabriela Boza-Moran,[1,2] Michel Cailleret,[1,2] Margot Jarrige,[1,2,3] Hélène Polvèche,[3] Jérôme Polentes,[3] Eric Chevet,[4,5] Cécile Martinat,[1,2] Marc Peschanski,[1,2,3] and Laetitia Aubry[1,2,*]

Summary

Recent studies indicate that neurodegenerative processes that appear during childhood and adolescence in individuals with Wolfram syndrome (WS) occur in addition to early brain development alteration, which is clinically silent. Underlying pathological mechanisms are still unknown. We have used induced pluripotent stem cell-derived neural cells from individuals affected by WS in order to reveal their phenotypic and molecular correlates. We have observed that a subpopulation of Wolfram neurons displayed aberrant neurite outgrowth associated with altered expression of axon guidance genes. Selective inhibition of the ATF6α arm of the unfolded protein response prevented the altered phenotype, although acute endoplasmic reticulum stress response—which is activated in late Wolfram degenerative processes—was not detected. Among the drugs currently tried in individuals with WS, valproic acid was the one that prevented the pathological phenotypes. These results suggest that early defects in axon guidance may contribute to the loss of neurons in individuals with WS.

Introduction

Wolfram syndrome (WS [MIM: 222300]) is a rare multi-systemic monogenic disease that is characterized by a panel of symptoms appearing during childhood and adolescence.[1] Focal neurodegenerative processes then occur, affecting neurosensory systems and the brainstem. Recent results of magnetic resonance imaging studies have revealed, however, that individuals affected by Wolfram syndrome display in addition a statistically significant overall reduction of brain volume. The origin of the brain volume reduction has been ascribed to yet unknown neurodevelopmental defects[2–4] because it is present as early as the authors looked for it and remains stable, in contrast to the later-appearing neurodegenerative processes that progress over time. This finding could be read in conjunction with older analyses of brains from WS-affected persons that had pointed-out widespread axonopathy[5] or diffuse leukoencephalopathy[6] in the absence of clinical correlates.

The molecular mechanisms that underlie WS, which results from mutations in *WFS1* (MIM: 606201) and consequently with the loss of wolframin protein, have been mainly ascribed to a defect in the stress response of the endoplasmic reticulum (ER).[7,8] This is supported by the localization of wolframin at the ER membrane[9] and its role as an inhibitor of the ATF6α branch of the unfolded protein response[10] (UPR). Accordingly, its absence in pancreatic β cells from individuals affected by WS has been associated with a defective control of the UPR leading to cell dysfunction and death[11] and diabetes. Defects in the ER stress response have also been proposed as the main pathological mechanism that leads to the progressive neurodegenerative processes that affect retinal ganglionic neurons and, by extension, sensory neurons of the ear and brainstem that also display strong losses over time.[12] Such phenomena were, however, difficult to reconcile with the spatial and temporal features of the overall reduction in brain volume.

In the present study, we sought to investigate the cellular and molecular mechanisms associated with the neurodevelopmental pathology in WS. We hypothesized that neurons differentiated from induced pluripotent stem cells (iPSCs) would provide us with a directly relevant experimental model in order to compare early neurodevelopmental phenomena from healthy and Wolfram donors. Protocols for the differentiation of pluripotent stem cells based upon the dual inhibition of both the activin/nodal and bone morphogenetic protein (BMP) pathways, the two canonical Smad-dependent pathways, have been shown to recapitulate nicely the progression of cells along the neural lineage.[13,14] In particular, glutamatergic cortical neurons can be specifically differentiated.[15] This has thus allowed us to compare similar neuronal populations from healthy and Wolfram donors at discrete early stages of neural development and reveal pathological abnormalities that provide clues to understand the mechanisms that lead to the defects in brain volume identified in individuals with WS.

[1]INSERM UMR 861, I-STEM, AFM, Corbeil-Essonnes 91100, France; [2]Université Paris-Saclay, INSERM, Univ Evry, Institut des Cellules Souches pour le Traitement et l'Étude des Maladies Monogéniques, Corbeil-Essonnes 91100, France; [3]CECS/AFM, I-STEM, Corbeil-Essonnes 91100, France; [4]INSERM U1242, Université Rennes 1, Rennes 35000, France; [5]Centre de Lutte Contre le Cancer Eugène Marquis, Rennes 35000, France
[6]These authors contributed equally
*Correspondence: laubry@istem.fr
https://doi.org/10.1016/j.ajhg.2021.10.001.

Material and methods

Fibroblast reprogramming and pluripotent stem cell culture

The CT1 and CT3 control iPSC lines have been reprogrammed at I-Stem and already published[15,16] (CT1 corresponding to line 1869 and CT3 to line PB12). The CT2 iPSC line was reprogrammed from IMR-90 lung fibroblast cell (ATCC CCL-186). WS1 and WS2 iPSC lines were kindly given by the New York Stem Cell Foundation and have already been published.[17] The WS5 iPSC line was derived from fibroblasts provided by Dr. Cécile Delettre and the late Professor Christian Hamel, isolated from one individual affected by WS biopsy after approval of the local ethical committee (NCT03853252, Institute for Neurosciences in Montpellier, France). All the cell lines used for this study as well as the experimental processes have been performed according to the French legal policy. Consequently, informed consent was obtained from all participants or their legal representatives.

Fibroblasts were grown in fibroblast culture medium consisting of DMEM high glucose (Invitrogen), GlutaMAX supplement (Invitrogen), supplemented with 10% fetal bovine serum (FBS, Sigma-Aldrich), 1% non-essential amino acids (Invitrogen), and 1 mM sodium pyruvate (Invitrogen). CT2 and WS5 iPSC lines were obtained and characterized as described by Yu et al.[18] with Addgene plasmid 20925, 20926, and 20927. iPSCs were grown on murine embryonic fibroblasts (MEFs) in human embryonic stem cells (hESCs) culture medium consisting of DMEM with 20% Knockout Serum Replacement (KSR), 1% non-essential amino acids, 1% GlutaMAX, 0.1% β-mercaptoethanol, and 0.1% penicillin/streptomycin (all from Thermo Fisher Scientific) and supplemented with 10 ng/mL FGF-2 (Peprotech) with manual passaging once a week and daily medium change during the characterization steps. They were then adapted for feeder-free culture and grown on vitronectin-coated dishes (Thermo Fisher Scientific) in StemMACS iPS-Brew XF (Miltenyi Biotec). Cultures were fed every 2 days and passaged every 5–7 days.

Pluripotent stem cell differentiation

For embryoid bodies (EBs) differentiation, iPSC colonies growing on MEFs were detached with 1 mg/mL collagenase (Thermo Fisher Scientific) during 10 min at 37°C, resuspended in hESCs medium without FGF-2, and cultured in low attachment 6-well plates for 7 days at 37°C and 5% CO_2. The EBs were then plated on 0.1% gelatin-coated (Sigma-Aldrich) plates and maintained for another 7 days prior immunostaining.

Neural stem cells (NSCs) differentiation was performed as described previously.[15] At this stage of differentiation, cells can be frozen in a 90% FBS/10% dimethylsulfoxyde ≥99.5% (DMSO, 0.005%, VWR) solution. After thawing, cells were seeded on a poly-L-ornithin/laminin (PO/LAM)-coated support in N2B27 medium consisting of DMEM/F12, neurobasal, N2 and B27 supplements, 0.1% β-mercaptoethanol, and 0.1% penicillin/streptomycin (all from Thermo Fisher Scientific) supplemented with 10 ng/mL of FGF-2 and epidermal growth factor (EGF) (Peprotech) and 10 μM of Y-27632 (StemCell Technologies). Medium was changed the next day without Y-27632 and then changed every 2 days. NSCs were passaged twice a week with Trypsin-EDTA 0.05% (Thermo Fisher Scientific) and seeded on PO/LAM-coated support at a density of 50,000 cells/cm^2 for amplification.

Neuronal differentiation was induced by plating the NSCs at low density (50,000 cells/cm^2) in PO/LAM-coated culture plates in N2B27 medium without FGF-2 and EGF. At day 4, we added 10 μM DAPT (R&D Systems) to the medium to stop cell proliferation. The medium was changed every 4 days and neurons were obtained after 18–21 days of *in vitro* (DIV) differentiation.

Drug treatments

For drug treatments experiments, NSCs were differentiated into neurons as previously described. The neurons were treated twice at DIV 10 and DIV 14 with the following molecules and concentrations:[19] 10 μM ceapin-A7 (Sigma-Aldrich); 2.5 μM MKC-8866 (Medinnovata); 10 μM salubrinal (Sigma-Aldrich); 100 nM liraglutide (Bio-Techne); 10 μM dantrolene (Sigma-Aldrich); 1 mM 4-phenyl butyric acid (4PBA, Merck); 0.5 mM or 1.5 mM valproic acid (VPA, Sigma-Aldrich). Ceapin-A7, MKC-886, salubrinal, liraglutide, and dantrolene were resuspended in DMSO. For further analyses, cultures were stopped at DIV 18. We used neuraminidase (NM) at 10 mU (Sigma-Aldrich) as a technical control to prevent the fasciculation as this enzyme removes specifically sialic acid residues and consequently reduces non-specifically adhesion between neurites.[20]

Ion AmpliSeq Transcriptome Human Gene Expression Kit

For each of the 12 samples, we reverse transcribed 50 ng of total RNA with the Ion AmpliSeq Transcriptome Human Gene Expression Kit by following the protocol of the manufacturer (Thermo Fisher Scientific).[21] The cDNA libraries were amplified and barcoded with Ion AmpliSeq Transcriptome Human Gene Expression core panel and Ion Xpress Barcode Adaptor (Thermo Fisher Scientific). The amplicons were quantified with the Agilent High Sensitivity DNA kit before the samples were pooled in sets of eight. Emulsion PCR and enrichment was performed on the Ion OT2 system Instrument with the Ion PI Hi-Q OT2 200 kit (Thermo Fisher Scientific). Samples were loaded on an Ion PI v.3 Chip and sequenced on the Ion Proton System with Ion PI Hi-Q sequencing 200 kit chemistry (200 bp read length; Thermo Fisher Scientific). The Ion Proton reads (FASTQ files) were imported into the RNA sequencing (RNA-seq) pipeline of Partek Flow software (v.6 Partek) with hg19 as a reference genome. The number of reads per sample ranged from 7.1 million to 10 million reads. To determine genes that are differentially expressed between groups, we quantified mapped reads by using Partek E/M algorithm after normalization by the total count/sample (the resulting counts represent the gene expression levels on reads/millions for over 20,800 different genes present in the AmpliSeq Human Gene Expression panel). Differentially expressed genes were identified via Partek gene-specific analysis (GSA) algorithm. Gene lists were filtered at p value ≤ 1%; |fold change| ≥ 1.5 minReads100. The use of p value instead of adjusted p value is justified by biological meaning and experimental validations (Figure S4C).[22] Biological interpretations of the list of differentially expressed genes were performed with dedicated software (Partek Genomics Suite [v.6.6] and the web-based gene list enrichment analysis tool EnrichR[23,24]). EnrichR analyses were performed on KEGG2016 database and GO biological process 2017b. AmpliSeq data produced in this study have been deposited on NCBI GEO under the accession number GEO: GSE156911.

Time-lapse imaging of neuronal differentiation

We seeded NSCs at 50,000 cells/cm^2 in PO/LAM-coated 384-well culture plates in N2B27 medium to induce neuronal differentiation. The plates were incubated in an IncuCyte Zoom Live Cell

Imaging System (Essen Bioscience), and phase contrast images were automatically taken under 10× microscopic magnification every 4 h for the first 2 weeks of differentiation and then every 12 h for the next 2 weeks. We extracted and piled up pictures by using the IncuCyte Zoom Software to create the movies.

WS5 rescued (WS5R) iPSC line generation

We generated the WS5R line by CRISPR-Cas9-mediated knockin to introduce *WFS1* cDNA, under a doxycycline inducible promoter, at the AAVS1 locus.

The homology-directed repair (HDR) donor plasmid was designed on the basis of the plasmid pAAVS1-PDi-CRISPRn (Addgene #73500). The Cas9 cassette was replaced with *WFS1* cDNA of the WFS1-pcDNA3 plasmid (Addgene #13011) via Gibson Assembly. The HDR donor plasmid includes homology arms at the 5′ and 3′ regions immediately flanking the DNA sequence of the AAVS1 locus to specifically direct integration of the vector into the AAVS1 locus. This plasmid is mainly composed of rtTA under pCAG promoter, PuroR under control of T2A peptide, and inducible TR3G promoter that allows the expression of *WFS1* with doxycycline treatment.

Prior to transfection, we performed the RNP complex formation by combining SpCas9 protein with the T2 guide RNA sequence 5′-GGGGCCACTAGGGACAGGAT-3′ that targets AAVS1 locus (ratio 1/1.2) (Integrated DNA Technologies, IDT).

WS5 iPSCs were first transfected with the linearized HDR donor plasmid with Lipofectamine 3000 (Thermo Fisher Scientific). Cells were transfected a second time with the *in vitro* preformed RNP complex with Lipofectamine CRISPRMAX (Thermo Fisher Scientific). The dual transfection has been realized following the manufacturer protocols. After transfection, the iPSCs were collected and plated in StemMACS iPS-Brew XF (Miltenyi Biotec) medium and 200 ng/mL puromycin (Thermo Fisher Scientific). The clones were selected after 1 week of culture.

WS5R iPSCs were differentiated into NSCs and neurons. In order to induce the production of wolframin, we treated NSCs with 50 ng/mL doxycycline (Sigma-Aldrich) at each medium change during 10 days. The 50 ng/mL doxycycline treatment was then maintained all along the differentiation into neurons.

Immunocytochemistry

Cells were fixed with 4% paraformaldehyde (Electron Microscopy Sciences) for 15 minutes at room temperature. Cells were then placed in a blocking buffer (phosphate-buffered saline, 2% bovine serum albumin, and 0.1% Triton X-100). Primary antibodies were diluted in blocking buffer and applied overnight at 4°C. Secondary antibodies conjugated to Alexa fluorophores (Thermo Fisher Scientific) were diluted at 1:1,000 in blocking buffer and applied for 1 h at room temperature in the dark. We applied Hoechst 33258 (Sigma-Aldrich) diluted at 1:3,000 in the same time to visualize the cell bodies. The cells were visualized on a Zeiss inverted fluorescence microscope and image acquisition was performed with the Zen blue software (Zeiss). When higher resolution was necessary, confocal imaging was performed with a Zeiss LSM880-Airyscan Confocal Microscope driven by the Zeiss Zen black software. The antibodies used are described in Table S2.

Immunostaining quantifications

Three biologically independent differentiations for each condition were investigated and five images at 20× magnification per each differentiation were quantified. Due to the high number of fibers on each image, the neurites thickness quantification was approached with a method of unbiased random sampling in ImageJ/FIJI. The method was based on the use of a grid (area per point: 8,000 μm^2) apposed automatically on the image by the software. A random third of the squares composing the grid were quantified for each image. On each counted square of the grid, neurite thickness was measured manually via the selection tool of imageJ for delimitation of the diameter of each fiber. ImageJ was then asked to measure the corresponding line length (i.e., the fiber thickness). The results for each image were then compiled on a global table to be classified in three arbitrary thickness intervals (0–3 μm, 3–6 μm, >6 μm). The same data were used for analysis of the mean thickness of the neuronal network for each condition.

To quantify the proportions/percentages of positive cells for each labeling, we used the CellInsight CX7 High-Content Screening (HCS) Platform and the HSC Studio software (Thermo Fisher Scientific). Based on the CX7-Colocalization Bioapplication and the acquisition of images at 10× magnification, a homemade algorithm had allowed the individual detection and quantification of nuclei (Hoechst), HuC/D (green) and CUX2 (red), and finally the calculation of the proportion of each labeling to the total number of cells, as quantitative readouts.

mRNA extraction and reverse-transcription (RT) PCR

Total RNA samples were isolated with the RNeasy Mini or Micro Plus extraction kit and QIAcube instrument (QIAGEN) according to the manufacturer's protocol. RNA quantification and quality were assessed with the NanoDrop ND-1000 spectrophotometer (Thermo Fisher Scientific) and the ND V33.7.1 software. The cDNA samples were synthetized from 500 ng of RNA with SuperScript III reverse transcriptase (Thermo Fisher Scientific) with a mix of 500 ng/μL random primers (Thermo Fisher Scientific) and 500 ng/μL Oligo(dT) (Thermo Fisher Scientific).

Quantitative PCR (qPCR)

qPCR assays were performed with Luminaris HiGreen qPCR Master Mix, low ROX (Thermo Fisher Scientific) with the QuantStudio 12K Flex Real-Time PCR System (Thermo Fisher Scientific) with hold stage (50°C for 2 min and 95°C for 10 min) followed by 40 cycles of denaturation (95°C for 15 s) and annealing (60°C for 1 min). Quantification of gene expression was based on the 2-ΔΔCt method and normalized to *18S* expression. Primers listed in Table S3 were used for gene expression.

Thapsigargin treatment

NSCs were seeded at 75,000 cells/cm^2 on PO/LAM-coated 6-well plates in N2B27 medium supplemented with 10 ng/mL of EGF and FGF-2 and incubated at 37°C, 5% CO_2 overnight. The next day, cells were treated with 50 nM of the non-competitive inhibitor of the sarco/endoplasmic reticulum Ca^{2+} ATPase (SERCA) thapsigargin (TG, Sigma-Aldrich). The cells were collected with RLT+ lysis buffer (QIAGEN) after 4 h, 6 h, and 8 h of treatment. For each time point, the control condition of DMSO was collected.

XBP1 gel analysis

RNA extraction and RT were performed as described above. For the *XBP1* splicing analysis, a PCR amplification was carried out with 0.05 U/μL recombinant Taq DNA polymerase (Thermo Fisher Scientific) and the primers listed in Table S3. The amplification was performed with a first step at 95°C for 5 min followed by 30 cycles of

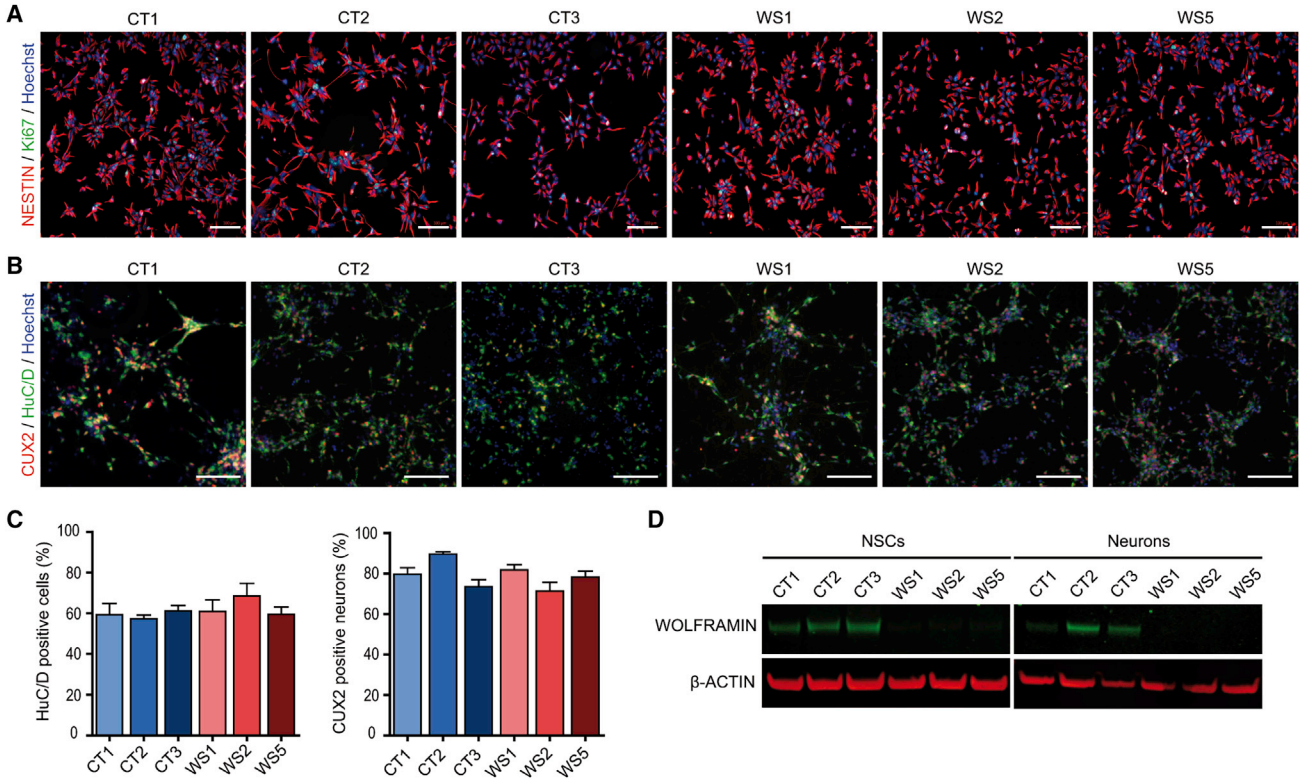

Figure 1. WS and CT iPSCs both efficiently generate homogeneous populations of neural stem cells and neurons
(A) Immunofluorescence microscopy for NESTIN (NSCs marker) and Ki67 (proliferation marker) in NSCs derived from the three control (CT1, CT2, and CT3) and the three WS (WS1, WS2, and WS5) iPSC lines. Scale bars, 100 μm.
(B) HuC/D- and CUX2-immunoreactive cortical neurons at days of *in vitro* (DIV) differentiation 14 from NSC stage. Scale bars, 100 μm.
(C) Proportion of HuC/D$^+$- and CUX2$^+$-immunoreactive neurons in cell culture at DIV 14 from NSC stage. Data are presented as mean ± SEM (n = 3 biologically independent differentiations. No statistical difference was observed via one-way ANOVA with Dunnett's post hoc test).
(D) Immunoblot of wolframin in NSCs and neurons at DIV 21.

denaturation (60 s at 95°C), followed by annealing step (30 s at 59°C) and finished by elongation step (30 s at 72°C) in the Eppendorf Mastercycler. The PCR products (spliced *XBP1* [*XBP1*s] and unspliced *XBP1* [*XBP1*u] at 193 pb and 223 pb, respectively) were quantified with the BioAnalyzer 2100 and the Agilent DNA 1000 kit (Agilent) according to the manufacturer's protocol. Spliced *XBP1* expression was normalized to total *XBP1* (*XBP1*s + *XBP1*u).

Western immunoblotting

Proteins samples were isolated from cell-lysates with radioimmunoprecipitation assay (RIPA) buffer (Sigma-Aldrich) supplemented with 1% protease inhibitors cocktail (Sigma-Aldrich) and 10% phosphatase inhibitor (Roche). Samples quantification was performed with Pierce BCA protein assay kit (Thermo Fisher Scientific) with CLARIOstar Plus instrument (BMG Labtech). The samples were prepared at a concentration of 30 μg of proteins and were placed 10 min at 70°C. Proteins were loaded on 4%–12% NuPAGE Bis-Tris gels (Thermo Fisher Scientific) with the Chameleon Duo Pre-stained Protein Ladder (Li-Cor) and migrated during 10 min at 50 mA and 40 min at 100 mA. The gels were then transferred onto nitrocellulose membranes (Thermo Fisher Scientific) via the iBlot 2 Dry Blotting System (Thermo Fisher Scientific). Blots were blocked for 1 h at room temperature in Odyssey Blocking Buffer (Li-Cor) and then incubated with primary antibody in the blocking buffer with 0.2% TWEEN 20 (Sigma-Aldrich) overnight at 4°C. Blots were then incubated with fluorescent secondary antibodies (1:10,000, Li-Cor) in the blocking buffer with 0.2% TWEEN 20 (Sigma-Aldrich) in the dark at room temperature for 1 h. The blots were revealed with Odyssey CLx Imaging System (Li-Cor). The antibodies used are described in Table S2.

Statistical analysis

All data were graphed and analyzed via GraphPad Prism 5 (GraphPad Software). Data shown are the mean ± SEM. Student's t tests were used for comparison between two groups. Group differences were analyzed with one-way analysis of variance (ANOVA) followed by Dunnett's multiple comparisons test.

Results

Six human iPSC lines were used in this study: three derived from healthy controls (CT1, CT2, and CT3) and three derived from individuals affected by WS with genetically and clinically identified Wolfram syndrome (WS1, WS2, and WS5). Information on CT and WS iPSCs are summarized in Table S1. All cell lines were validated with classical assays for stemness, pluripotency, and genomic integrity (Figures S1A–S1C). WS-proliferating neural stem cells (NSCs) and post-mitotic neurons showed an absence of wolframin protein unlike all CT cells (Figure 1 and Figure S1E).

WS neurons display impaired neurite outgrowth

When CT and WS cell lines were differentiated along the neural lineage, no difference in terms of detection of the NSCs markers, NESTIN and SOX2, and that of the cortical neurons markers, HuC/D and CUX2, as well as the total number of cells, was observed between both types of lines (Figures 1A–1C and Figure S1D). In contrast, TUJ1 immunostaining in neurites revealed a striking morphological difference between CT and WS cells. Indeed, CT neurons formed a typical stellate array of thin branching fibers, whereas WS cells exhibited long and large processes (up to several millimeters in length) without apparent branching (Figure 2A and Figures S2A and S2D). Using confocal microscopy, these large processes appeared to be formed by the aggregation of parallel neurites bundled together (Figure 2B). Live-cell imaging revealed that those abnormal neurite figures appeared between days 10 and 14 of neuronal differentiation *in vitro* (DIV), depending on the cell line (Videos S1, S2, S3, and S4). In WS neuronal cultures, neuritic bundles built up progressively while neurites were growing straight through the culture without apparent interaction with cell clusters. Processes grew longer and larger over about a week, after which the neuritic networks remained stable. In addition, the growing tips of some of the neuritic bundles formed unusual U-turns and even full circles (Figure S2B).

As a way to quantify the phenomenon, we measured the thickness of isolated and bundled neurites in CT and WS cultures. Although most of the above-mentioned structures were below 3 μm in size in both CT and WS cells, WS cells exhibited a smaller number of those thin processes than CT. Conversely, the number of neurites bundles were both more abundant and larger in WS cells, reaching up to 58 μm in width while CT neuritic structures did not exceed 12 μm. Consequently, the mean thickness of neuritic structures was higher in WS neurons than in the CT (Figure 2C). To further compare WS and CT cells, we defined three thickness intervals (0–3 μm, 3–6 μm, and >6 μm) and observed that >90% of the CT neuritic structures ranged in the 0–3 μm interval while this proportion was significantly reduced to about 80% in WS cells (Figure 2D and Figure S2C). Conversely, there was less than 1% neuritic structures per mm^2 with a thickness >6 μm in CT, whereas this number was up to 10% in WS cells (Figures 2D and 2E and Figure S2C). These results indicate that the absence of wolframin leads to aberrant neurite outgrowth, which in turn could impact on neural functionality.

Restoration of wolframin normalizes neurite outgrowth in WS neurons

To confirm that the absence of wolframin was involved in the neuritic phenotype, we generated a *WFS1*-rescued WS iPSC line by using CRISPR-Cas9 gene-editing to introduce the *WFS1* cDNA under a doxycycline-inducible promoter at the AAVS1 locus (the WS5 line was used; Figure 3A). Pluripotent characteristics and normal karyotype were maintained in the rescued iPSC line (WS5R) (Figures S3A and S3B). Successful gene editing was confirmed after 50 ng/mL doxycycline (Dox) treatment as wolframin synthesis was detected in NSCs and neurons (Figure 3B). WS5R cells differentiated similarly to the parental WS5 line into NSCs (Figure S3C). Moreover, expression of *WFS1* upon treatment with 50 ng/mL Dox did not alter the percentage of HuC/D^+ and $CUX2^+$ neurons (Figures 3C and 3D), thus indicating that the initial properties of the cell line were not altered by the expression of the transgene. In sharp contrast, Dox-mediated induction of *WFS1* expression changed the neuritic network (Figure 3E), restoring it to what was observed in CT cells. Typical stellate arrays of thin neurites extending between clusters of cells were observed in the Dox-treated cultures. Quantification of isolated and bundled neurites per mm^2 showed a normalization of the profile that closely resembled CT cultures (Figures 3G and 3H and Figure S3D). We observed similar results for the mean thickness (Figure 3F). As a control, doxycycline treatment in non-engineered WS5 neurons did not affect markers of differentiation and was also ineffective on neuritic outgrowth (Figures S3E–S3G), demonstrating that the normalization of the neuritic network by doxycycline treatment required the presence of the *WFS1* construct.

WS cells exhibit defects in the expression of genes involved in neurodevelopment and axon guidance

Global gene expression was compared between CT and WS NSCs and neurons. In a principal-component analysis (PCA), the samples clustered on the basis of their phenotype (CT NSCs, WS NSCs, CT neurons, and WS neurons) (Figure 4A). In contrast, the two groups, CT and WS, differed in the number of differentially expressed genes (DEGs) (p value $\leq$ 1%; fold change $\geq$ 1.5; minReads100). There were 493 DEGs for WS compared to CT NSCs (249 upregulated and 244 downregulated) and 254 DEGs for WS neurons in comparison to CT neurons (87 upregulated and 167 downregulated). Among these DEGs, 29 were commonly dysregulated in WS NSCs and neurons (Figure S4A). When DEGs in neurons were mapped to Kyoto Encyclopedia of Genes and Genomes (KEGG) pathways, the most significantly enriched pathway was "axon guidance" (Figure 4B). Functional annotation revealed that the top three significantly enriched gene ontology categories were "neurogenesis," "nervous system development," and "axon guidance" (Figure 4B). In WS cells, axon growth and guidance-related genes were either upregulated, such as roundabout-1 (*ROBO1* [MIM: 602430]), or downregulated, such as slit guidance ligand 3 (*SLIT3* [MIM: 603745]), semaphorin 4A (*SEMA4A* [MIM: 607292]), tenascin C (*TNC* [MIM: 187380]), and several ephrins (*EPHs*). DEGs associated with those categories were also downregulated at the NSC state, such as Unc-5 netrin receptor D (*UNC5D* [MIM: 616466]), growth-associated protein 43 (*GAP43* [MIM: 162060]), the ephrin type-B receptor 1 (*EPHB1* [MIM: 600600]), or *TNC* (Figure S4B). Results

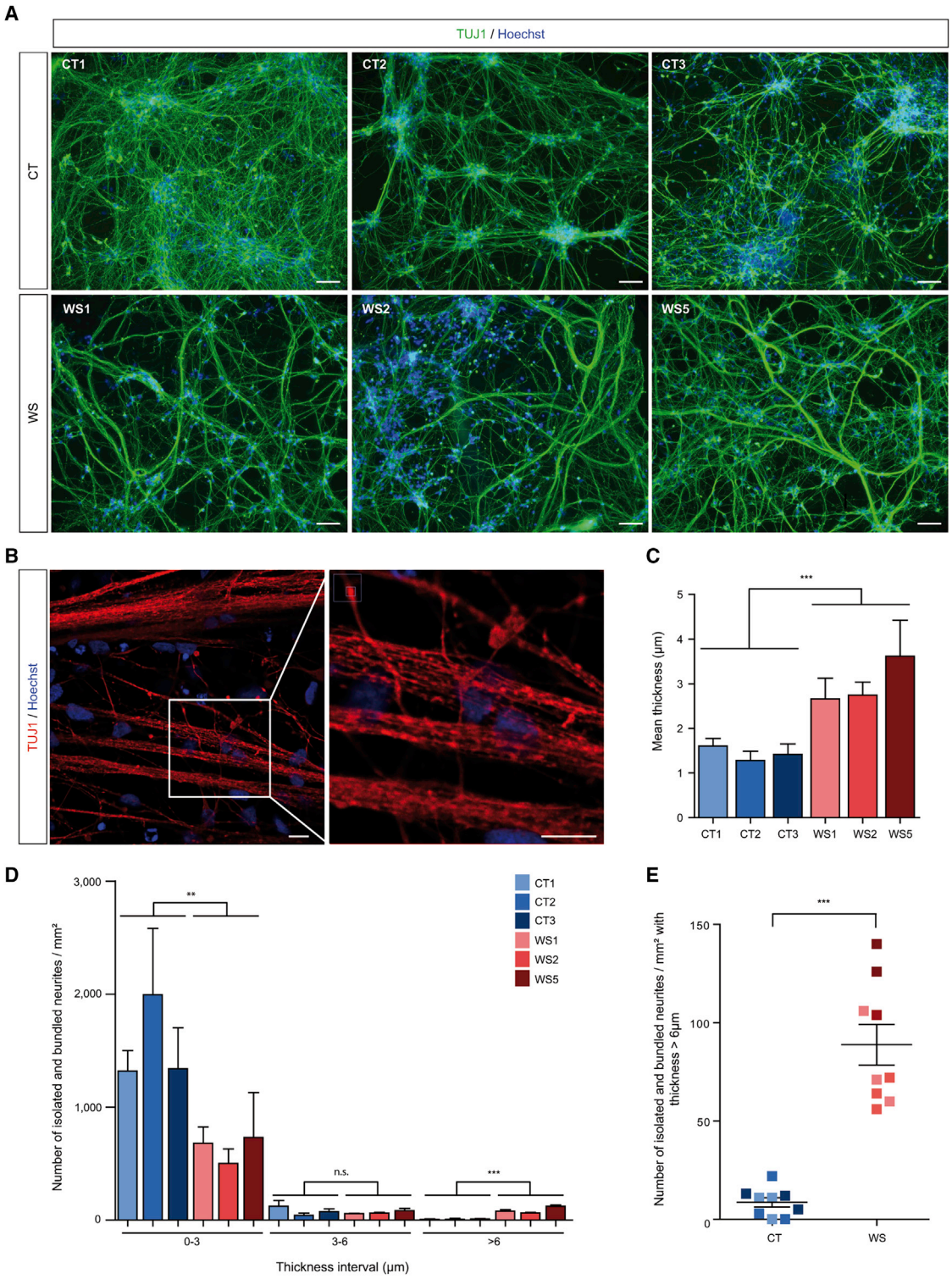

Figure 2. WS neurons display abnormal neurite outgrowth

(A) TUJ1-immunoreactive CT and WS neurons at DIV 21. Scale bars, 100 µm.

(B) Confocal analysis of TUJ1-immunoreactive WS5 neurons at DIV 21. Scale bars, 10 µm.

(C) Quantification of the mean thickness of isolated and bundled neurites in CT and WS neurons.

(D) Quantification of the number of isolated and bundled neurites per mm^2 over three thickness intervals (0–3, 3–6, and >6 µm) for CT and WS neurons (see material and methods).

(E) Quantification of the mean number of isolated and bundled neurites for CT and WS neurons in the >6 µm interval of thickness. The color code indicating the different cell lines is common to (C), (D), and (E). All the data are presented as mean ± SEM (n = 3 biologically independent differentiations; **$p < 0.01$, ***$p < 0.001$; Student's t test).

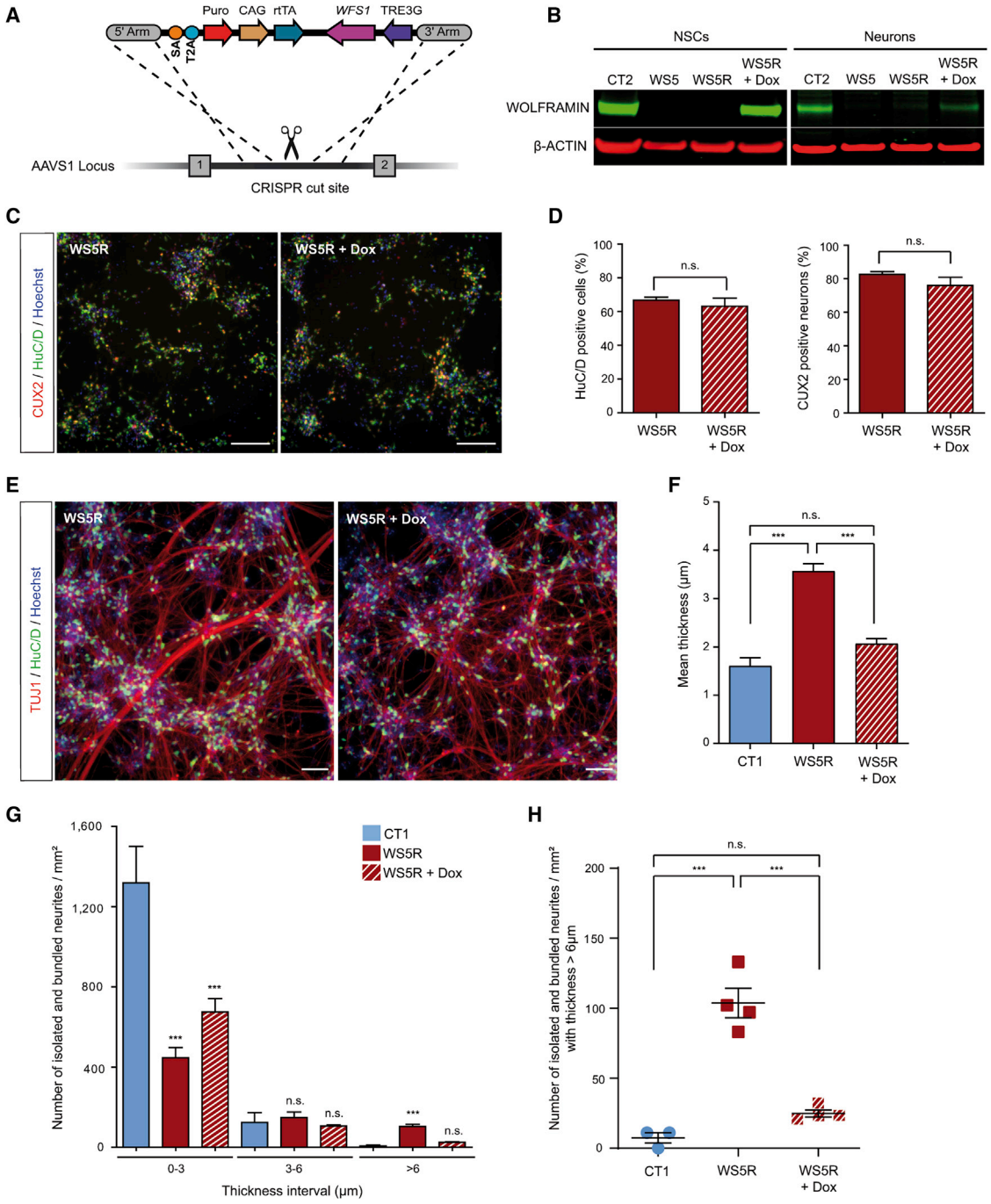

Figure 3. *WFS1* cDNA knockin rescues phenotype in WS neurons at DIV 21

(A) Gene editing strategy with CRISPR-Cas9 technology for insertion at the AAVS1 locus of *WFS1* cDNA under a doxycycline inducible promoter in WS5 iPSC line.

(B) Immunoblot detection of wolframin in rescued WS5 (WS5R) NSCs and neurons with or without doxycycline (Dox) treatment and in CT2.

(C) HuC/D and CUX2 immunostaining of WS5R neurons treated or not with Dox. Scale bars, 100 µm.

(D) Proportion of HuC/D$^+$- and CUX2$^+$-immunoreactive cells in WS5R neurons treated or not with Dox. Data are presented as mean ± SEM (n = 3 biologically independent differentiations; Student's t test).

(E) TUJ1- and HuC/D-immunoreactive WS5R neurons treated or not with Dox. Scale bars, 100 µm.

(F) Quantification of the mean thickness of isolated and bundled neurites for WS5R neurons treated or not with Dox compared to CT1.

(G) Quantification of the number of isolated and bundled neurites per mm^2 for three thickness intervals (0–3, 3–6, and >6 µm) in neurons.

(H) Analysis of the number of isolated and bundled neurites per mm^2 for the >6 µm interval in WS5R neurons treated or not with Dox compared to CT1. For (F), (G), and (H), data are expressed relative to that of CT1 cells and presented as mean ± SEM (n = 3 for CT1 and n = 4 for WS5R and WSR5 + Dox biologically independent differentiations; ***p < 0.001; one-way ANOVA with Dunnett's post hoc test, data are compared to CT1 cells).

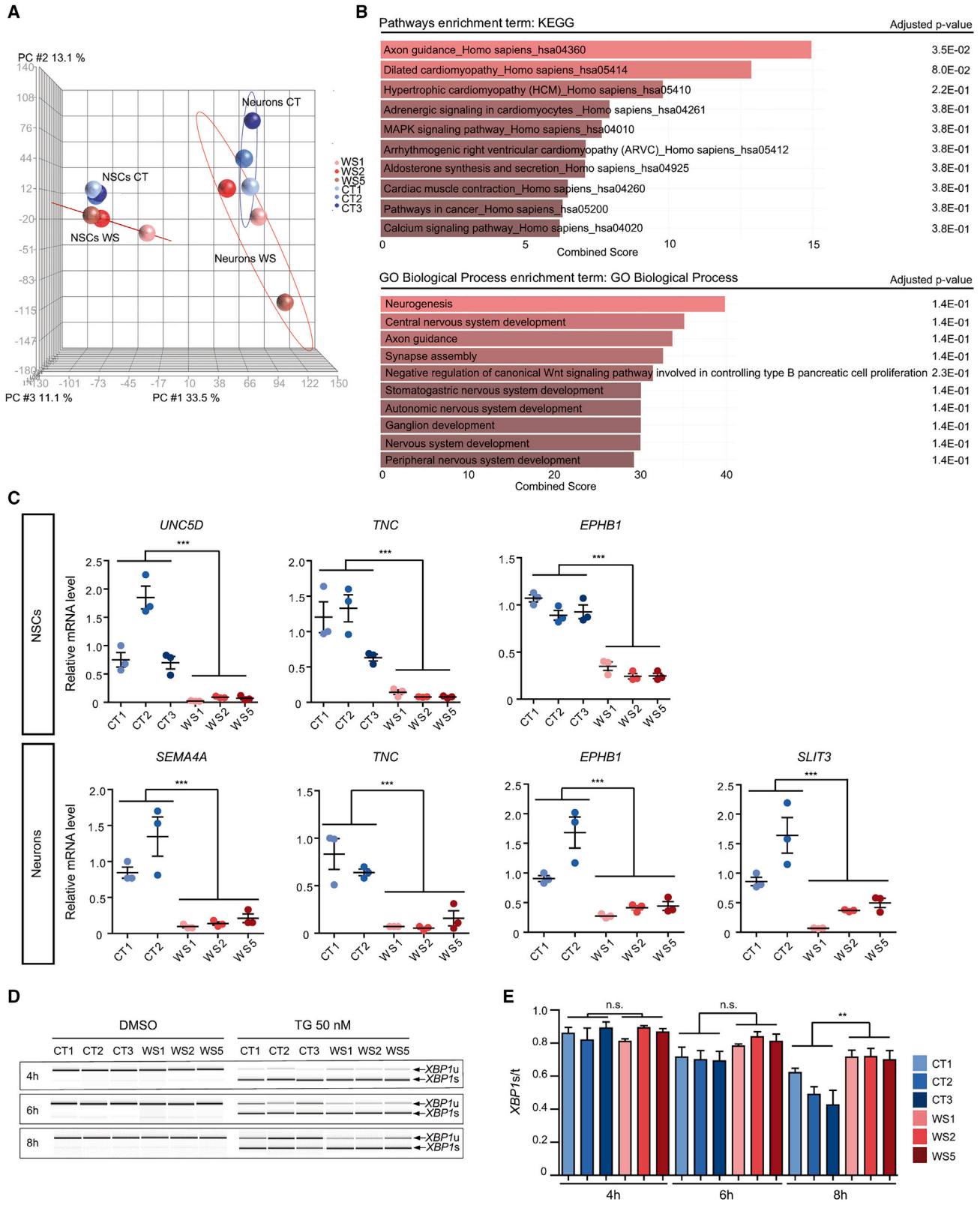

Figure 4. Global gene expression comparison between CT and WS NSCs and neurons

(A and B) Transcriptome analysis with AmpliSeq. (A) Principal-component analysis (PCA) between CT and WS NSCs and neurons. (B) KEGG pathways (upper panel) and gene ontology (lower panel) enrichment analysis in neurons via Enrichr tool.

(C) Quantitative RT-PCR analysis of DEGs mRNA levels in CT and WS NSCs and neurons. Data are expressed relative to that of CT1 cells and normalized to *18S* rRNA expression. Data are presented as mean ± SEM (n = 3 biologically independent differentiations; ***$p < 0.001$; Student's t test).

(legend continued on next page)

were confirmed for a set of genes by qRT-PCR (Figure 4C). Altogether, these data suggest that a neurite outgrowth program is deregulated in WS neurons.

Taking into account the literature that associates degeneration processes in Wolfram with the activation of the unfolded protein response (UPR),[11] we specifically analyzed the expression of selected UPR target genes. Under basal (and vehicle) condition, no difference between CT and WS NSCs was detected (Figures S4C and S4D). In contrast, activation of the ER stress response by treating the cells with 50 nM thapsigargin (TG) revealed a slower return to baseline of the splicing of X-box-binding protein 1 (*XBP1* [MIM: 194355]) mRNA in WS than in CT, indicating that WS cells could be more sensitive to ER stress (Figures 4D and 4E). These results suggest that UPR signaling might be affected in WS cells and may lead to chronic and low intensity signaling alterations resulting in turn into pathological phenotypes.

Pharmacological rescue of WS neurons and potential mechanisms of action

To test the latter hypothesis, we sought to investigate how the three branches of the UPR could contribute to the identified neuritic phenotype by using selective pharmacological inhibitors. With this approach, neither IRE1α inhibition (via MKC-8866) nor alteration of the integrated stress response (ISR, via salubrinal) elicited any change of the abnormal neuritic network of WS cells (Figures 5A–5F and Figures S5A–S5G). In contrast, inhibition of the ATF6α branch of the UPR with 10 μM ceapin-A7 rescued neurites formation by WS cells during neuronal differentiation. Ceapin-A7-treated WS cell cultures showed neuritic networks that closely resembled CT cultures in terms both of the number of neuritic structures in the interval superior to 6 μm of thickness (Figures 5G–5I and Figures S5H–S5J) and of the mean thickness (2.162 ± 0.256 μm for NT versus 1.265 ± 0.177 μm for ceapin-A7). These results suggest the existence of non-conventional (non-acute) signaling ATF6 mechanisms in WS cells that may lead to aberrant neuritic structures and that are blunted by ceapin-A7.

Valproic acid treatment has positive effects on neurite outgrowth and axon guidance genes in WS neurons

In the same line of thought, the effects of various drugs that are currently being tested in individuals with WS or under preclinical study, namely the calcium modulator dantrolene, the GLP1 agonist liraglutide, and the HDAC inihibitors 4-phenylbutyric acid (4PBA) and valproic acid (VPA, also described as an ER stress signaling attenuator), were evaluated on the pathological neurite outgrowth phenotype. Neuraminidase (NM) was used as a control because this enzyme reduces non-specific adhesion between neurites. Accordingly, 10 mU NM prevented the formation of fascicles in WS neurons when applied at the beginning of the post-mitotic neuronal differentiation (Figure 6A). NM had no effect on global genes expression. There was no difference in neurite outgrowth defects between treated and non-treated WS cell cultures when using either 100 nM liraglutide, 1 mM 4PBA, or 10 μM dantrolene (Figure S6A). In contrast, 1.5 mM VPA-treated WS cells demonstrated a change in the abnormal neuritic phenotype, displaying a profile comparable to those of NM-treated WS neurons (Figure 6A). WS neurons treated with that dose showed a neuritic network similar to CT neurons in terms both of isolated and bundled fibers (Figures 6B–6D and Figure S6B). In parallel, VPA increased the expression of *SLIT3*, *TNC*, and *EPHB1*, three of the axon guidance genes that are downregulated in WS cells (Figure 6E). VPA had no impact on either the number of cells or the proportion of HuC/D^{+} neurons in the cultures, precluding a toxic effect (Figures S6C and S6D). In contrast, attempts at correcting the pathological phenotype after it was installed by starting the VPA treatment at DIV 18 were ineffective. As a search for additional clues concerning molecular mechanisms, VPA was tested for a protective effect on the prolonged thapsigargin-induced ER stress response observed in WS NSCs. There was no protection elicited by this drug. Valproic acid thus demonstrated a preventive effect on the neurite outgrowth abnormality observed in WS neurons, the mechanism of which is unrelated to a protection against an abnormal ER stress response.

Discussion

The main result of the present study is the demonstration that human iPSC-derived neurons with Wolfram syndrome-associated mutations display phenotypic and molecular neurodevelopmental defects. This reveals as an alteration of the neuritic outgrowth and axonal pathfinding, together with abnormally extensive fasciculation in culture. Changes in gene expression concerned a set of genes involved in neurodevelopment and axonal pathfinding. It may be speculated that these pathological alterations participate to the reduction of brain volume in individuals affected by WS. Although the expression of genes encoding proteins involved in the acute response to UPR was not altered, WS cells appeared more sensitive to ER stress. Among the currently explored therapeutic candidates, only valproic acid demonstrated an ability to alleviate some of the observed neurodevelopmental defects in WS neurons.

The results of our study shed some light on a series of clinical results that appeared up to now paradoxical. Indeed, progressive neurodegenerative alterations pertaining to Wolfram syndrome, which affect several neurosensory

(D and E) ER stress induction in CT and WS NSCs after 4, 6, and 8 h of 50 nM thapsigargin (TG) treatment. (D) Analysis of the expression of spliced (*XBP1*s) and unspliced (*XBP1*u) *XBP1*. (E) Quantification of *XBP1*s expression normalized to total *XBP1* (*XBP1*t). Data are presented as mean ± SEM (n = 3 biologically independent experiments; *$p < 0.05$; one-way ANOVA with Dunnett's post hoc test).

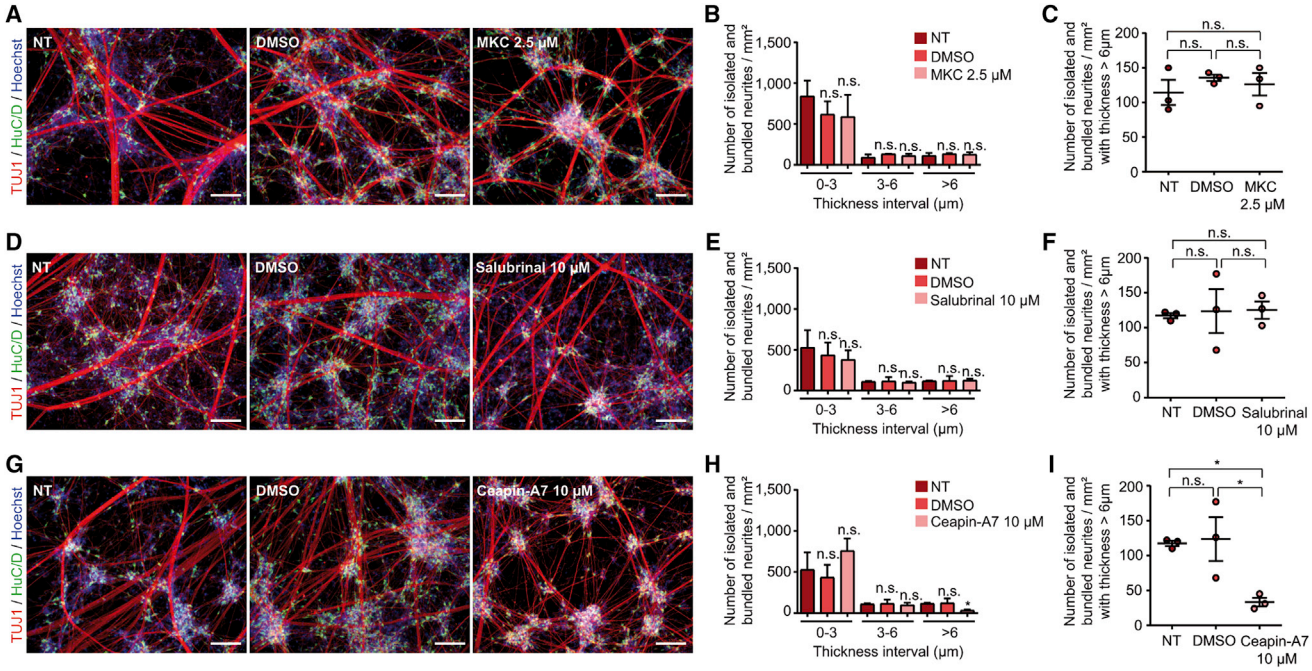

Figure 5. Effect of the inhibition of each of the three branches of UPR pathways on the neurite outgrowth defect in WS5 neurons
(A, B, and C) Inhibition of IRE1α pathway with 2.5 μM MKC-8866 (MKC). (A) TUJ1 and HuC/D immunostaining of WS5 neurons at DIV 18 after MKC or control DMSO treatments. Scale bars, 100 μm. (B) Quantification of the number of isolated and bundled neurites per mm^2 for three thickness intervals (0–3, 3–6, and >6 μm) in WS5 neurons treated or not with MKC or control DMSO. (C) Quantification of the number of isolated and bundled neurites for the >6 μm interval in WS5 neurons treated or not with MKC or control DMSO.
(D, E, and F) Same representation for the inhibition of integrated stress response with 10 μM salubrinal.
(G, H, and I) Same representation for the inhibition of ATF6 pathway with 10 μM ceapin-A7. For all analyses, data are presented as mean ± SEM (n = 3 biologically independent differentiations; *p < 0.05; one-way ANOVA with Dunnett's post hoc test, data are compared to non-treated cells [NTs]).

pathways,[2,7,25] the brainstem, and cerebellum,[5,26] appear only several years after birth (in childhood and adolescence) and progress over time. However, these phenomena, which have dramatic clinical correlates, are preceded by an overall decrease in brain volume, both in gray and white matters, as recently demonstrated by a series of MRI studies.[3,4] These alterations were observed very early on in life and did not evolve with age, suggesting a neurodevelopmental defect previously ignored because it is clinically silent.[12] Consistent with that observation, neurodevelopmental brain alterations were also observed in animal models of the disease.[27–29] Our *in vitro* cell culture results may well provide a mechanistic basis for those early neurodevelopmental alterations. Indeed, a proportion of WS neurons exhibited neurite outgrowth abnormalities that may make them unsuitable for elaborating normal sets of connections, ultimately being consequential for neuronal survival.[30] Thick bundled neurites displayed trajectories that were not similar to those observed in CT cell cultures, extending over very long distances without apparent attraction toward cell bodies and forming curves or even full loops. Time-lapse imaging revealed a concomitant alteration of guiding cues at the tip of the bundled neurites. These phenotypic changes were coherently associated with a prevalent dysregulation of a set of genes that belong to the "axon guidance" subset. Among the most dysregulated genes were *SLIT3*, *SEMA4A*, *UNCD5*, *TNC*, *GAP43*, *ROBO1*, and several *EPHRINS* that all encode proteins that are necessary for axonal pathfinding and whose defect is associated with major neurodevelopmental abnormalities.[31,32] Different studies have described a potential link between axonal pathfinding defects and reduced brain volume both in murine models and in persons.[33–36] The precise mechanisms by which the dysregulation of the expression of those genes may lead to reduced brain volumes in individuals with Wolfram syndrome remain however to be fully established.

Most of the dysregulated genes that are referred to above are encoding proteins either located at the plasma membrane or exerting their functions extracellularly. As such, they require functional biogenesis pathways, which encompass the secretory pathway. Interestingly, wolframin has been shown to act as a regulator of the ER homeostasis master regulator, namely the unfolded protein response, and pathological mechanisms associated to Wolfram syndrome have been largely ascribed to a defective control of those processes due to the loss of wolframin.[10] In our model, there was no difference between the expression at baseline of any of the acute ER stress markers in neural cells derived from either CT or WS iPSC lines, in contrast to what has been reported for pancreatic β cells.[17,37] It is only when ER stress was elicited by thapsigargin that WS NSCs demonstrated a prolonged

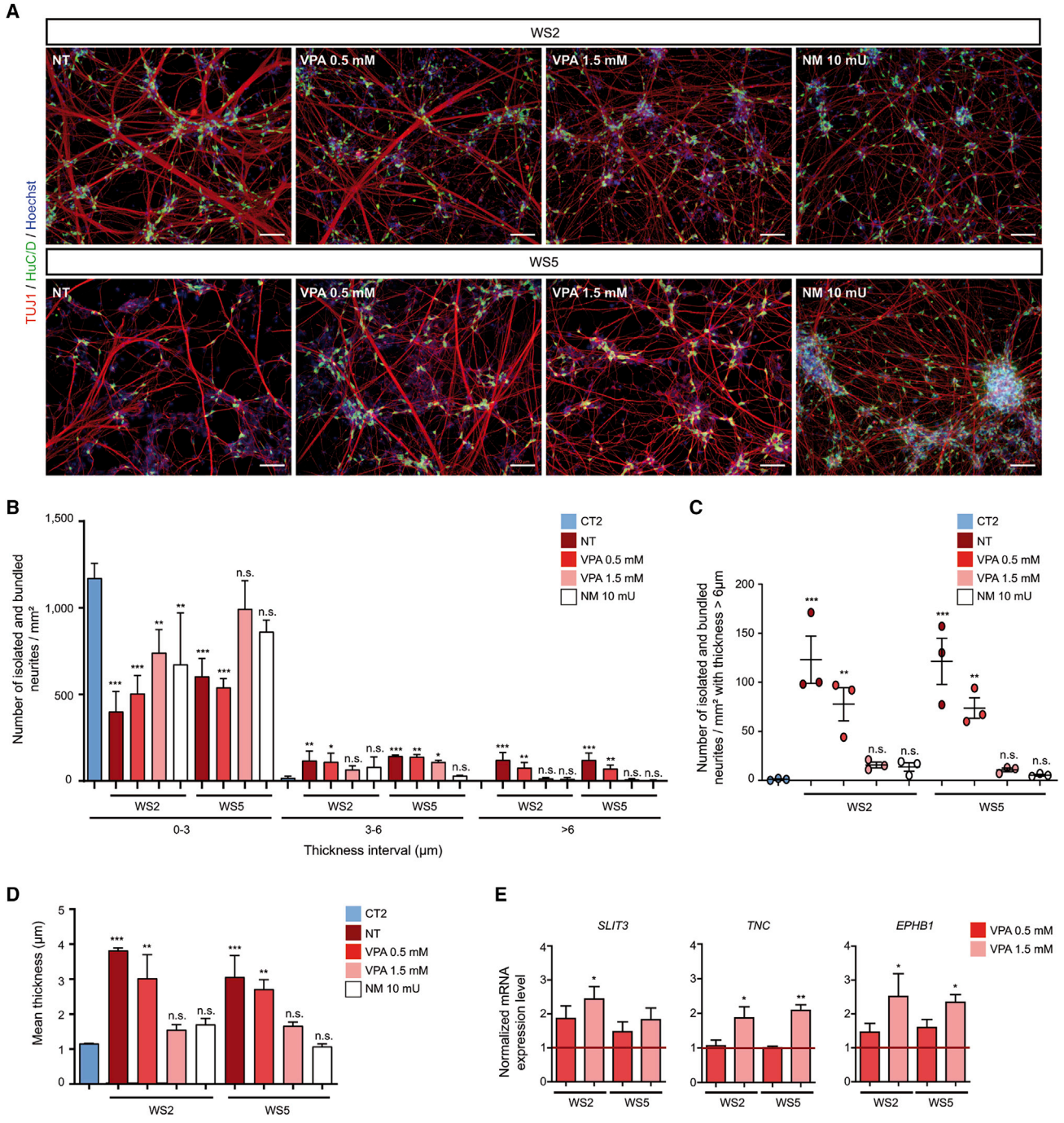

Figure 6. Valproic acid (VPA) treatment prevents abnormal neurite outgrowth in WS neurons

(A) TUJ1 and HuC/D immunostaining of WS2 and WS5 neurons at DIV 18 without (NT) or after 0.5 or 1.5 mM VPA or 10 mU neuraminidase (NM) treatment. Scale bars, 100 µm.

(B) Quantification of the number of isolated and bundled neurites per mm^2 for three thickness intervals (0–3, 3–6, and >6 µm) in WS2 and WS5 neurons treated or not with 0.5 or 1.5 mM VPA or 10 mU NM.

(C) Quantification of the number of isolated and bundled neurites for the >6 µm interval in WS2 and WS5 neurons treated or not with 0.5 or 1.5 mM VPA or 10 mU NM.

(D) Quantification of the mean thickness of isolated and bundled neurites for WS2 and WS5 neurons treated or not with 0.5 or 1.5 mM VPA or 10 mU NM. For (B), (C), and (D), data are expressed relative to that of CT2 cells.

(E) Quantitative RT-PCR analysis of *SLIT3*, *TNC*, and *EPHB1* transcript levels in WS2 and WS5 neurons treated with 0.5 or 1.5 mM VPA. Data are expressed relative to that of non-treated cells (NTs) and normalized to *18S* rRNA expression. For all analyses, data are presented as mean ± SEM (n = 3 biologically independent differentiations; *p < 0.05, **p < 0.01, ***p < 0.001; one-way ANOVA with Dunnett's post hoc test, data are compared to CT2 cells).

activation of *XBP1* mRNA splicing as compared to CT, thus indicative of a reduced ability of those cells to cope with prolonged ER stress. These results suggest that, even though under basal conditions canonical ER stress markers are not detected, ER homeostasis appears to be affected in WS neural cells. This hypothesis was confirmed when the WS-associated phenotype was blunted upon treatment with ceapin-A7, an ATF6 inhibitor.[38] Since wolframin was shown to inhibit ATF6 activation,[10] our results suggest that neurite development may be impacted on by a constitutive/chronic activation of ATF6 in WS cells that may lead to an alteration of both ER homeostasis and capacity to handle stress in those cells.

The observation of a clear pathological phenotype associated to altered gene expression markers in neural cells *in vitro* prompted us to analyze the potential therapeutic effects of drugs that are currently under preclinical or clinical study. The landscape of assayed treatments for Wolfram syndrome is, indeed, particularly rich, promoted by the observation of a number of potentially treatable functional defects.[1,39] The demonstrated loss of calcium cell homeostasis[40,41] has thus led to a clinical trial based upon the ER calcium stabilizer dantrolene (NCT02829268). In parallel, the nonselective histone deacetylase inhibitor valproic acid (VPA) is currently tested in clinical trial (NCT03717909) after being shown to reverse the defective production of $P21^{cip}$ in *WFS1* knockout cells.[42] Other drugs under preclinical study include GLP1-agonists such as liraglutide, which showed neuroprotective in Wolfram cell models in addition to its expected effect on insulin secretion,[43,44] and the chemical chaperone with antioxidant activity 4-PBA.[39] In our model, only VPA demonstrated a dose-dependent preventive action on the aberrant neurite outgrowth, and this was associated with the normalization of the expression of genes encoding axon guidance proteins. VPA has been shown to reduce ER stress,[45] and this may participate to its positive effects on WS neurons. Alternatively, one may hypothesize a less-specific effect because VPA is a very potent non-specific histone deacetylase inhibitor that impacts well over one thousand genes in neural cells *in vitro*.[46] As a pleiotropic neuroactive drug, it is known to exert neuroprotective effects in a wide array of models of neurodegenerative diseases, including amyotrophic lateral sclerosis,[47] Parkinson disease,[48] or spinal cord injury.[49] Of particular interest for the interpretation of our data are the results of two studies that explored the promotion of neurite outgrowth by VPA in two models of neural defects due to different CMT mutations, Rab7 in CMT2B[50] and AARS in CMT2N.[51] The fact that VPA appeared to promote neurite outgrowth in similar fashion in pathological models based on different gene mutations strongly suggests that those drug effects were not specific to a discrete pathological mechanism. Nevertheless, our data support the hypothesis that VPA may help alleviate some symptoms in individuals with Wolfram syndrome, which is currently tried in the clinic.

Whether the identified neurodevelopmental defects in axonal pathfinding may be associated after years with the observed neurodegenerative phenomena or whether neurodevelopmental and neurodegenerative processes are due to independent pathological mechanisms is at this stage but a matter of speculation. It is worth mentioning, however, that a link between such differentially timed defects has been hypothesized by several authors over the past 10 years for other late-appearing neurodegenerative diseases. In a seminal review, Lin and co-workers[52] underlined the fact that genome-wide analyses for Parkinson disease revealed that single-nucleotide polymorphisms in axon-guidance genes were predictive of different Parkinson disease outcomes. This was further extended to other neurodegenerative diseases[53] and, in particular, impaired axonal sprouting was hypothetically associated to dysregulation of axon guidance proteins in amyotrophic lateral sclerosis. Axonal pathfinding is fundamental for the establishment of proper connectivity and functionality of neurons in the adult central nervous system. It has been proposed that dysregulation of developmental processes requiring axon guidance may be compensated to a certain point in time but later lead to degeneration.[52–55] Conversely, subtle defects in proteins that play a role not only during neurodevelopment but also in adult neuroplasticity may contribute to delayed neurodegeneration.

Data and code availability

The transcriptomic datasets generated during this study are available at NCBI GEO under the accession number GEO: GSE156911 (https://www.ncbi.nlm.nih.gov/geo/query/acc.cgi?acc=GSE156911).

Supplemental information

Supplemental information can be found online at https://doi.org/10.1016/j.ajhg.2021.10.001.

Acknowledgments

I-Stem is part of the Biotherapies Institute for Rare Diseases (BIRD) supported by the Association Française contre les Myopathies (AFM-Téléthon). This project was also supported by grants from Association Syndrome de Wolfram, Association Nationale de la Recherche et de la Technologie, and Agence Nationale pour la Recherche: NeurATRIS ANR-11-INBS-0011 and Labex REVIVE ANR-10-LABX-73. M.-G.B.-M. was supported by the program "investissement d'avenir" INGESTEM. We thank Yolande Masson and Lina El Kassar for karyotyping the cell lines and Alexandre Carteron for the technical support with the AmpliSeq experiments. We thank Cécile Delettre and the late Christian Hamel (Institut des Neurosciences de Montpellier) for the gift of the WS5 fibroblasts and the New York Stem Cell Foundation for WS1 and WS2 iPSC lines. We thank Ole Isacson (Harvard Medical School) for advice and reading the manuscript and Nathalie Holic for advice with genome editing. We gratefully acknowledge support from the PSMN (Pôle Scientifique de Modélisation Numérique) of the ENS de Lyon for computing resources.

Declaration of interests

The authors declare no competing interests.

Received: May 20, 2021
Accepted: September 30, 2021
Published: October 25, 2021

Web resources

OMIM, https://omim.org/

References

1. Pallotta, M.T., Tascini, G., Crispoldi, R., Orabona, C., Mondanelli, G., Grohmann, U., and Esposito, S. (2019). Wolfram syndrome, a rare neurodegenerative disease: from pathogenesis to future treatment perspectives. J. Transl. Med. *17*, 238.
2. Hershey, T., Lugar, H.M., Shimony, J.S., Rutlin, J., Koller, J.M., Perantie, D.C., Paciorkowski, A.R., Eisenstein, S.A., Permutt, M.A.; and Washington University Wolfram Study Group (2012). Early brain vulnerability in Wolfram syndrome. PLoS ONE *7*, e40604.
3. Lugar, H.M., Koller, J.M., Rutlin, J., Marshall, B.A., Kanekura, K., Urano, F., Bischoff, A.N., Shimony, J.S., Hershey, T.; and Washington University Wolfram Syndrome Research Study Group (2016). Neuroimaging evidence of deficient axon myelination in Wolfram syndrome. Sci. Rep. *6*, 21167.
4. Lugar, H.M., Koller, J.M., Rutlin, J., Eisenstein, S.A., Neyman, O., Narayanan, A., Chen, L., Shimony, J.S., and Hershey, T. (2019). Evidence for altered neurodevelopment and neurodegeneration in Wolfram syndrome using longitudinal morphometry. Sci. Rep. *9*, 6010.
5. Shannon, P., Becker, L., and Deck, J. (1999). Evidence of widespread axonal pathology in Wolfram syndrome. Acta Neuropathol. *98*, 304–308.
6. Chaussenot, A., Bannwarth, S., Rouzier, C., Vialettes, B., Mkadem, S.A., Chabrol, B., Cano, A., Labauge, P., and Paquis-Flucklinger, V. (2011). Neurologic features and genotype-phenotype correlation in Wolfram syndrome. Ann. Neurol. *69*, 501–508.
7. Barrett, T.G., Bundey, S.E., and Macleod, A.F. (1995). Neurodegeneration and diabetes: UK nationwide study of Wolfram (DIDMOAD) syndrome. Lancet *346*, 1458–1463.
8. Rohayem, J., Ehlers, C., Wiedemann, B., Holl, R., Oexle, K., Kordonouri, O., Salzano, G., Meissner, T., Burger, W., Schober, E., et al. (2011). Diabetes and neurodegeneration in Wolfram syndrome: a multicenter study of phenotype and genotype. Diabetes Care *34*, 1503–1510.
9. Takeda, K., Inoue, H., Tanizawa, Y., Matsuzaki, Y., Oba, J., Watanabe, Y., Shinoda, K., and Oka, Y. (2001). WFS1 (Wolfram syndrome 1) gene product: predominant subcellular localization to endoplasmic reticulum in cultured cells and neuronal expression in rat brain. Hum. Mol. Genet. *10*, 477–484.
10. Fonseca, S.G., Ishigaki, S., Oslowski, C.M., Lu, S., Lipson, K.L., Ghosh, R., Hayashi, E., Ishihara, H., Oka, Y., Permutt, M.A., and Urano, F. (2010). Wolfram syndrome 1 gene negatively regulates ER stress signaling in rodent and human cells. J. Clin. Invest. *120*, 744–755.
11. Fonseca, S.G., Fukuma, M., Lipson, K.L., Nguyen, L.X., Allen, J.R., Oka, Y., and Urano, F. (2005). WFS1 is a novel component of the unfolded protein response and maintains homeostasis of the endoplasmic reticulum in pancreatic beta-cells. J. Biol. Chem. *280*, 39609–39615.
12. Samara, A., Rahn, R., Neyman, O., Park, K.Y., Samara, A., Marshall, B., Dougherty, J., and Hershey, T. (2019). Developmental hypomyelination in Wolfram syndrome: new insights from neuroimaging and gene expression analyses. Orphanet J. Rare Dis. *14*, 279.
13. Chambers, S.M., Fasano, C.A., Papapetrou, E.P., Tomishima, M., Sadelain, M., and Studer, L. (2009). Highly efficient neural conversion of human ES and iPS cells by dual inhibition of SMAD signaling. Nat. Biotechnol. *27*, 275–280.
14. Boissart, C., Nissan, X., Giraud-Triboult, K., Peschanski, M., and Benchoua, A. (2012). miR-125 potentiates early neural specification of human embryonic stem cells. Development *139*, 1247–1257.
15. Boissart, C., Poulet, A., Georges, P., Darville, H., Julita, E., Delorme, R., Bourgeron, T., Peschanski, M., and Benchoua, A. (2013). Differentiation from human pluripotent stem cells of cortical neurons of the superficial layers amenable to psychiatric disease modeling and high-throughput drug screening. Transl. Psychiatry *3*, e294.
16. Darville, H., Poulet, A., Rodet-Amsellem, F., Chatrousse, L., Pernelle, J., Boissart, C., Héron, D., Nava, C., Perrier, A., Jarrige, M., et al. (2016). Human Pluripotent Stem Cell-derived Cortical Neurons for High Throughput Medication Screening in Autism: A Proof of Concept Study in SHANK3 Haploinsufficiency Syndrome. EBioMedicine *9*, 293–305.
17. Shang, L., Hua, H., Foo, K., Martinez, H., Watanabe, K., Zimmer, M., Kahler, D.J., Freeby, M., Chung, W., LeDuc, C., et al. (2014). β-cell dysfunction due to increased ER stress in a stem cell model of Wolfram syndrome. Diabetes *63*, 923–933.
18. Yu, J., Hu, K., Smuga-Otto, K., Tian, S., Stewart, R., Slukvin, I.I., and Thomson, J.A. (2009). Human induced pluripotent stem cells free of vector and transgene sequences. Science *324*, 797–801.
19. Hetz, C., Axten, J.M., and Patterson, J.B. (2019). Pharmacological targeting of the unfolded protein response for disease intervention. Nat. Chem. Biol. *15*, 764–775.
20. Wakade, C.G., Mehta, S.H., Maeda, M., Webb, R.C., and Chiu, F.C. (2013). Axonal fasciculation and the role of polysialic acid-neural cell adhesion molecule in rat cortical neurons. J. Neurosci. Res. *91*, 1408–1418.
21. Li, W., Turner, A., Aggarwal, P., Matter, A., Storvick, E., Arnett, D.K., and Broeckel, U. (2015). Comprehensive evaluation of AmpliSeq transcriptome, a novel targeted whole transcriptome RNA sequencing methodology for global gene expression analysis. BMC Genomics *16*, 1069.
22. Amrhein, V., Greenland, S., and McShane, B. (2019). Scientists rise up against statistical significance. Nature *567*, 305–307.
23. Chen, E.Y., Tan, C.M., Kou, Y., Duan, Q., Wang, Z., Meirelles, G.V., Clark, N.R., and Ma'ayan, A. (2013). Enrichr: interactive and collaborative HTML5 gene list enrichment analysis tool. BMC Bioinformatics *14*, 128.
24. Kuleshov, M.V., Jones, M.R., Rouillard, A.D., Fernandez, N.F., Duan, Q., Wang, Z., Koplev, S., Jenkins, S.L., Jagodnik, K.M., Lachmann, A., et al. (2016). Enrichr: a comprehensive gene set enrichment analysis web server 2016 update. Nucleic Acids Res. *44* (W1), W90-7.
25. Carson, M.J., Slager, U.T., and Steinberg, R.M. (1977). Simultaneous occurrence of diabetes mellitus, diabetes insipidus, and optic atrophy in a brother and sister. Am. J. Dis. Child. *131*, 1382–1385.

26. Scolding, N.J., Kellar-Wood, H.F., Shaw, C., Shneerson, J.M., and Antoun, N. (1996). Wolfram syndrome: hereditary diabetes mellitus with brainstem and optic atrophy. Ann. Neurol. *39*, 352–360.
27. Cagalinec, M., Liiv, M., Hodurova, Z., Hickey, M.A., Vaarmann, A., Mandel, M., Zeb, A., Choubey, V., Kuum, M., Safiulina, D., et al. (2016). Role of Mitochondrial Dynamics in Neuronal Development: Mechanism for Wolfram Syndrome. PLoS Biol. *14*, e1002511.
28. Plaas, M., Seppa, K., Reimets, R., Jagomäe, T., Toots, M., Koppel, T., Vallisoo, T., Nigul, M., Heinla, I., Meier, R., et al. (2017). Wfs1- deficient rats develop primary symptoms of Wolfram syndrome: insulin-dependent diabetes, optic nerve atrophy and medullary degeneration. Sci. Rep. *7*, 10220.
29. Sakakibara, Y., Sekiya, M., Fujisaki, N., Quan, X., and Iijima, K.M. (2018). Knockdown of wfs1, a fly homolog of Wolfram syndrome 1, in the nervous system increases susceptibility to age- and stress-induced neuronal dysfunction and degeneration in Drosophila. PLoS Genet. *14*, e1007196.
30. Zweifel, L.S., Kuruvilla, R., and Ginty, D.D. (2005). Functions and mechanisms of retrograde neurotrophin signalling. Nat. Rev. Neurosci. *6*, 615–625.
31. Wang, L., and Marquardt, T. (2013). What axons tell each other: axon-axon signaling in nerve and circuit assembly. Curr. Opin. Neurobiol. *23*, 974–982.
32. Roig-Puiggros, S., Vigouroux, R.J., Beckman, D., Bocai, N.I., Chiou, B., Davimes, J., Gomez, G., Grassi, S., Hoque, A., Karikari, T.K., et al. (2020). Construction and reconstruction of brain circuits: normal and pathological axon guidance. J. Neurochem. *153*, 10–32.
33. Engle, E.C. (2010). Human genetic disorders of axon guidance. Cold Spring Harb. Perspect. Biol. *2*, a001784.
34. Hibar, D.P., Stein, J.L., Jahanshad, N., Kohannim, O., Hua, X., Toga, A.W., McMahon, K.L., de Zubicaray, G.I., Martin, N.G., Wright, M.J., et al. (2015). Genome-wide interaction analysis reveals replicated epistatic effects on brain structure. Neurobiol. Aging *36* (*Suppl 1*), S151–S158.
35. Vosberg, D.E., Zhang, Y., Menegaux, A., Chalupa, A., Manitt, C., Zehntner, S., Eng, C., DeDuck, K., Allard, D., Durand, F., et al. (2018). Mesocorticolimbic Connectivity and Volumetric Alterations in *DCC* Mutation Carriers. J. Neurosci. *38*, 4655–4665.
36. Deloulme, J.C., Gory-Fauré, S., Mauconduit, F., Chauvet, S., Jonckheere, J., Boulan, B., Mire, E., Xue, J., Jany, M., Maucler, C., et al. (2015). Microtubule-associated protein 6 mediates neuronal connectivity through Semaphorin 3E-dependent signalling for axonal growth. Nat. Commun. *6*, 7246.
37. Urano, F. (2014). Wolfram syndrome iPS cells: the first human cell model of endoplasmic reticulum disease. Diabetes *63*, 844–846.
38. Gallagher, C.M., and Walter, P. (2016). Ceapins inhibit ATF6α signaling by selectively preventing transport of ATF6α to the Golgi apparatus during ER stress. eLife *5*, e11880.
39. Abreu, D., and Urano, F. (2019). Current Landscape of Treatments for Wolfram Syndrome. Trends Pharmacol. Sci. *40*, 711–714.
40. Lu, S., Kanekura, K., Hara, T., Mahadevan, J., Spears, L.D., Oslowski, C.M., Martinez, R., Yamazaki-Inoue, M., Toyoda, M., Neilson, A., et al. (2014). A calcium-dependent protease as a potential therapeutic target for Wolfram syndrome. Proc. Natl. Acad. Sci. USA *111*, E5292–E5301.
41. Cagalinec, M., Zahradníková, A., Zahradníková, A., Jr., Kováčová, D., Paulis, L., Kureková, S., Hot'ka, M., Pavelková, J., Plaas, M., Novotová, M., and Zahradník, I. (2019). Calcium Signaling and Contractility in Cardiac Myocyte of Wolframin Deficient Rats. Front. Physiol. *10*, 172.
42. Gharanei, S., Zatyka, M., Astuti, D., Fenton, J., Sik, A., Nagy, Z., and Barrett, T.G. (2013). Vacuolar-type H+-ATPase V1A subunit is a molecular partner of Wolfram syndrome 1 (WFS1) protein, which regulates its expression and stability. Hum. Mol. Genet. *22*, 203–217.
43. Kondo, M., Tanabe, K., Amo-Shiinoki, K., Hatanaka, M., Morii, T., Takahashi, H., Seino, S., Yamada, Y., and Tanizawa, Y. (2018). Activation of GLP-1 receptor signalling alleviates cellular stresses and improves beta cell function in a mouse model of Wolfram syndrome. Diabetologia *61*, 2189–2201.
44. Seppa, K., Toots, M., Reimets, R., Jagomäe, T., Koppel, T., Pallase, M., Hasselholt, S., Krogsbæk Mikkelsen, M., Randel Nyengaard, J., Vasar, E., et al. (2019). GLP-1 receptor agonist liraglutide has a neuroprotective effect on an aged rat model of Wolfram syndrome. Sci. Rep. *9*, 15742.
45. Li, Z., Wu, F., Zhang, X., Chai, Y., Chen, D., Yang, Y., Xu, K., Yin, J., Li, R., Shi, H., et al. (2017). Valproate Attenuates Endoplasmic Reticulum Stress-Induced Apoptosis in SH-SY5Y Cells via the AKT/GSK3β Signaling Pathway. Int. J. Mol. Sci. *18*, 315.
46. Fukuchi, M., Nii, T., Ishimaru, N., Minamino, A., Hara, D., Takasaki, I., Tabuchi, A., and Tsuda, M. (2009). Valproic acid induces up- or down-regulation of gene expression responsible for the neuronal excitation and inhibition in rat cortical neurons through its epigenetic actions. Neurosci. Res. *65*, 35–43.
47. Wang, X., Ma, M., Teng, J., Che, X., Zhang, W., Feng, S., Zhou, S., Zhang, Y., Wu, E., and Ding, X. (2015). Valproate Attenuates 25-kDa C-Terminal Fragment of TDP-43-Induced Neuronal Toxicity via Suppressing Endoplasmic Reticulum Stress and Activating Autophagy. Int. J. Biol. Sci. *11*, 752–761.
48. Harrison, I.F., Crum, W.R., Vernon, A.C., and Dexter, D.T. (2015). Neurorestoration induced by the HDAC inhibitor sodium valproate in the lactacystin model of Parkinson's is associated with histone acetylation and up-regulation of neurotrophic factors. Br. J. Pharmacol. *172*, 4200–4215.
49. Chu, T., Zhou, H., Lu, L., Kong, X., Wang, T., Pan, B., and Feng, S. (2015). Valproic acid-mediated neuroprotection and neurogenesis after spinal cord injury: from mechanism to clinical potential. Regen. Med. *10*, 193–209.
50. Yamauchi, J., Torii, T., Kusakawa, S., Sanbe, A., Nakamura, K., Takashima, S., Hamasaki, H., Kawaguchi, S., Miyamoto, Y., and Tanoue, A. (2010). The mood stabilizer valproic acid improves defective neurite formation caused by Charcot-Marie-Tooth disease-associated mutant Rab7 through the JNK signaling pathway. J. Neurosci. Res. *88*, 3189–3197.
51. Tatsumi, Y., Matsumoto, N., Iibe, N., Watanabe, N., Torii, T., Sango, K., Homma, K., Miyamoto, Y., Sakagami, H., and Yamauchi, J. (2019). CMT type 2N disease-associated AARS mutant inhibits neurite growth that can be reversed by valproic acid. Neurosci. Res. *139*, 69–78.
52. Lin, L., Lesnick, T.G., Maraganore, D.M., and Isacson, O. (2009). Axon guidance and synaptic maintenance: preclinical

markers for neurodegenerative disease and therapeutics. Trends Neurosci. *32*, 142–149.

53. Van Battum, E.Y., Brignani, S., and Pasterkamp, R.J. (2015). Axon guidance proteins in neurological disorders. Lancet Neurol. *14*, 532–546.

54. Stoeckli, E. (2017). Where does axon guidance lead us? F1000Res. *6*, 78.

55. Schwamborn, J.C. (2018). Is Parkinson's Disease a Neurodevelopmental Disorder and Will Brain Organoids Help Us to Understand It? Stem Cells Dev. *27*, 968–975.

The American Journal of Human Genetics, Volume *108*

Supplemental information

Human iPSC-derived neurons reveal early developmental alteration of neurite outgrowth in the late-occurring neurodegenerative Wolfram syndrome

Sandra Pourtoy-Brasselet, Axel Sciauvaud, Maria-Gabriela Boza-Moran, Michel Cailleret, Margot Jarrige, Hélène Polvèche, Jérôme Polentes, Eric Chevet, Cécile Martinat, Marc Peschanski, and Laetitia Aubry

Supplemental Data

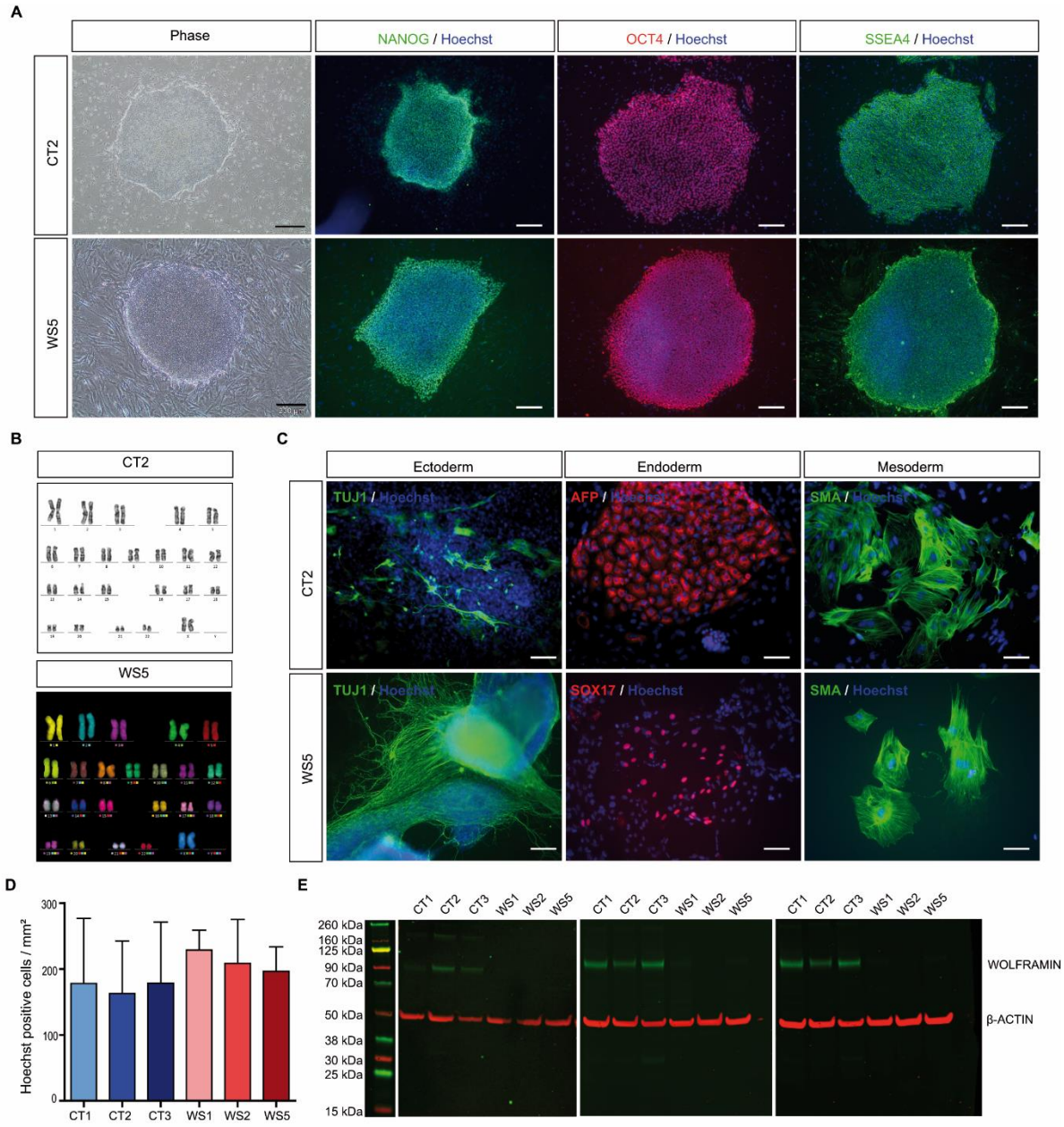

Figure S1: Characterization of CT2 and WS5 iPSC lines and quantification of the number of cells in CT and WS neuronal culture. A. Phase contrast images of CT2 and WS5 iPSCs and immunostaining of the pluripotency markers NANOG, OCT4 and SSEA4. Scale bars, 200 µm. **B.** G-banding and mFISH (46, XX). **C.** Three germ layer differentiation in *in vitro* embryoid bodies. Scale bars, 200 µm. **D.** Quantification of the number of cells (Hoechst) in CT and WS neuronal culture at DIV 14 from NSC stage. **E.** Western blot images of wolframin in CT and WS neurons at DIV 21 (related to Figure 1D for left panel; n = 3 biologically independent differentiations).

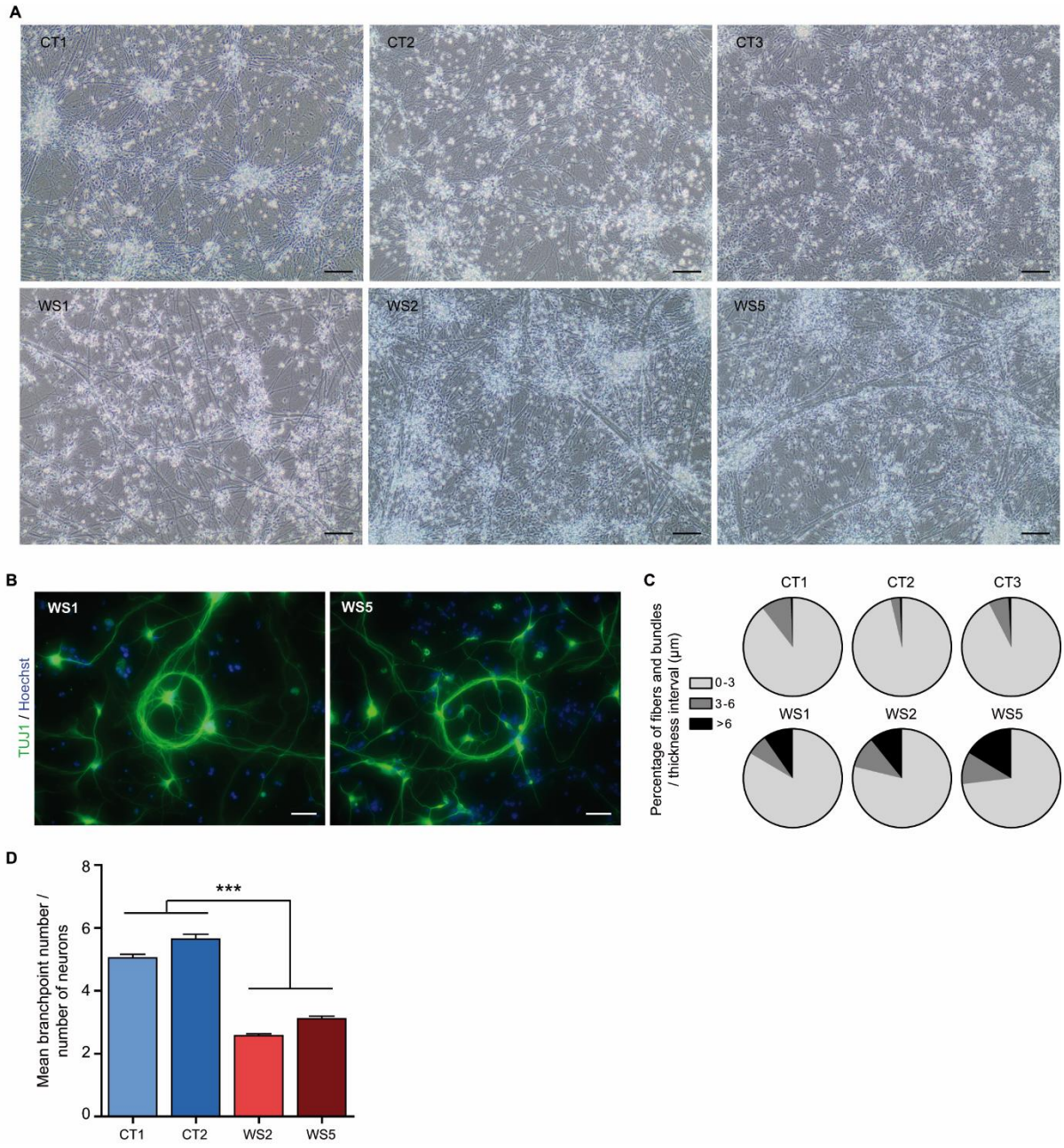

Figure S2: Abnormal neurite outgrowth in WS neurons. A. Phase contrast images of CT and WS neuronal network at DIV 14. Scale bars, 200 µm. **B.** TUJ1 immunostained loop structures. Scale bars, 50 µm. **C.** Proportion of isolated and bundled neurites for three thickness intervals (0 - 3; 3 - 6 and > 6 µm) in CT and WS neurons. **D.** Mean branchpoint number per number of neurons. Data are presented as mean ± SEM (n = 1 differentiation; 43 technical replicats; ***p < 0.001; Student's t-test).

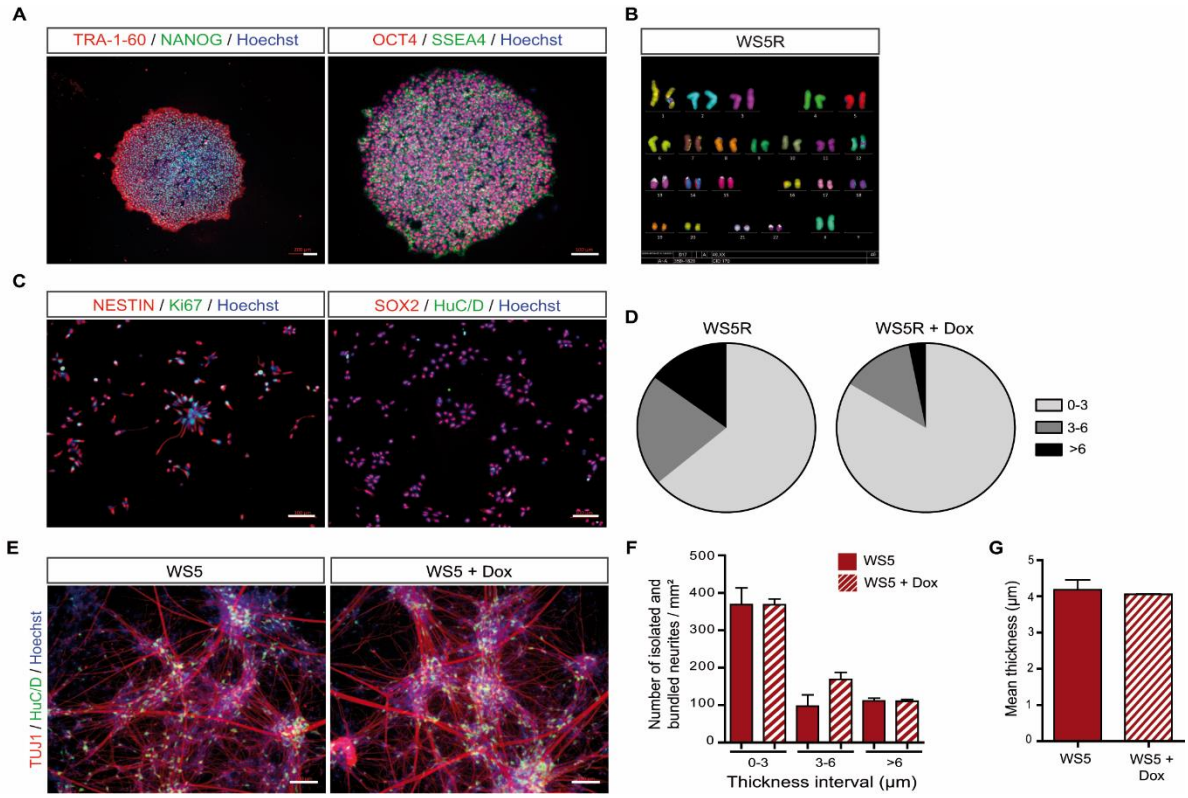

Figure S3: Characterization of WS5 rescue (WS5R) iPSCs, NSCs and neurons. A. Characterization of WS5R iPSCs by immunostaining of the pluripotency markers TRA-1-60, NANOG, OCT4, SSEA4. Scale bars, 100 µm**. B.** mFISH chromosome analysis of WS5R iPSC line showing a normal karyotype (46, XX). **C.** Immunostaining of the neural (NESTIN and SOX2), the neuronal (HuC/D) and the proliferation (Ki67) markers in WS5R-derived NSCs. Scale bars, 100 µm. **D.** Proportion of isolated and bundled neurites per each thickness interval (0 - 3; 3 - 6 and > 6 µm) of WS5R neurons at DIV 21. **E.** TUJ1 and HuC/D immunostaining of the parental WS5 neurons at DIV 21 under doxycycline (Dox) treatments. Scale bars, 100 µm. **F.** Quantification of the number of isolated and bundled neurites per mm^2 for each thickness interval (0 - 3; 3 - 6 and > 6 µm) at DIV 21 in the parental WS5 neurons treated with doxycycline. Data are presented as mean ± SEM (n = 3 biologically independent differentiations; No statistical difference was observed using one-way ANOVA with Dunnett's post hoc test). **G.** Mean thickness of the parental WS5 neurons at DIV 21 under doxycycline treatments. Data are presented as mean ± SEM (n = 3 biologically independent differentiations; No statistical difference was observed using Student's t-test).

A

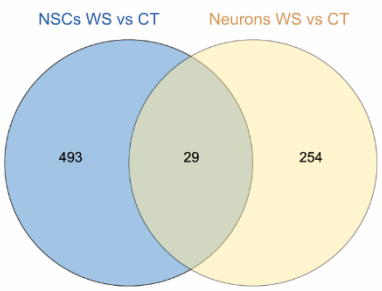

B

NSCs			Neurons		
Gene ID	P-value (WS vs CT)	Fold change (WS vs CT)	Gene ID	P-value (WS vs CT)	Fold change (WS vs CT)
UNC5D	4,51E-05	-2,57E+01	*ROBO1*	2,93E-06	3,01E+00
GAP43	2,48E-04	-7,54E+00	*SEMA4A*	4,57E-03	-5,15E+01
TNC	1,57E-03	-5,77E+00	*SLIT3*	1,41E-03	-6,07E+00
EPHB1	2,45E-03	-3,35E+00	*TNC*	2,29E-03	-5,91E+00
			EPHA8	1,98E-03	1,62E+01
			EPHB1	1,02E-03	-2,81E+00
			EFNB3	4,45E-03	-1,82E+00

C

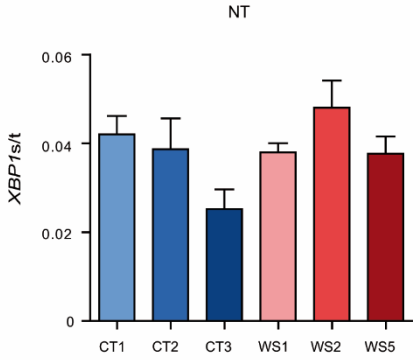

D

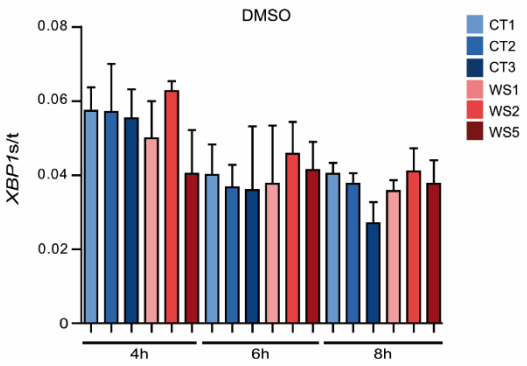

Figure S4: Gene expression analysis between CT and WS NSCs and neurons. A. Venn diagram summarizing the number of DEGs specific or common to NSCs and neurons. **B.** Table of axon guidance genes deregulated in WS NSCs and neurons. **C. and D.** Controls of thapsigargin (TG) treatments. Quantification of *XBP1s* expression normalized to total *XBP1* (*XBP1t*) in non-treated (**C**) and in DMSO treated (**D**) CT and WS NSCs after 4, 6 and 8 hours. Data are presented as mean ± SEM (n = 3 biologically independent experiments; *p<0.05; No statistical difference was observed using one-way ANOVA with Dunnett's post hoc test).

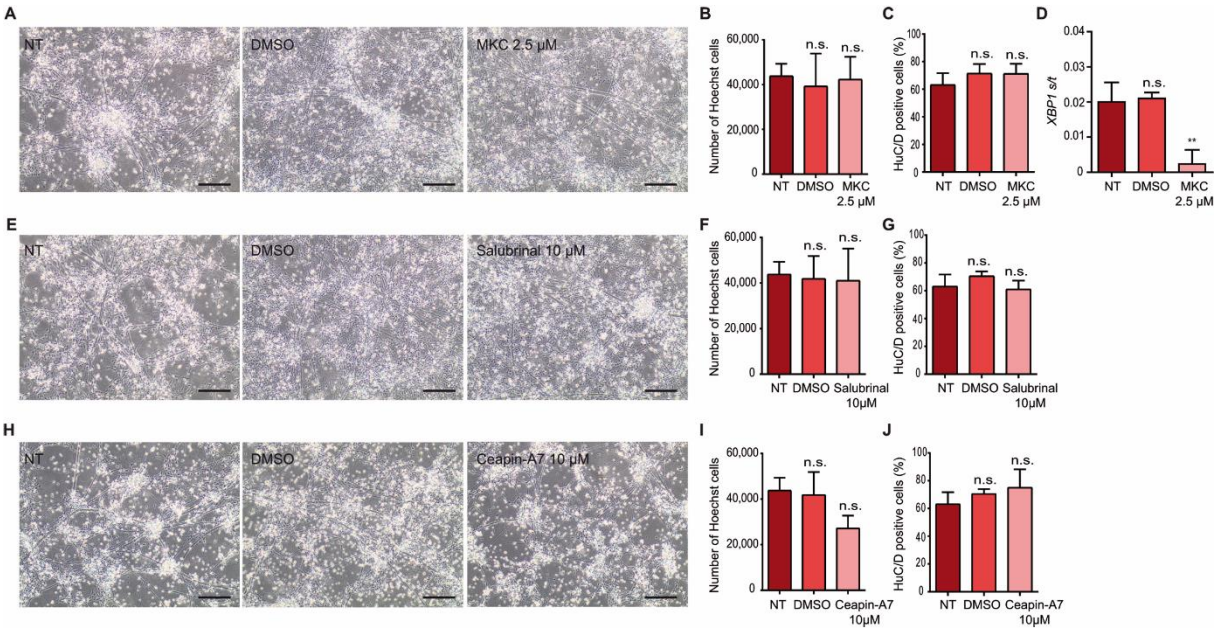

Figure S5: Effect of UPR pathways inhibition on the abnormal neurite outgrowth in WS5 neurons. **A.** Phase contrast images of WS5 neurons at DIV 18 treated or not with 2.5 µM MKC-8866 (MKC) or control DMSO. Scale bars, 200 µm. **B.** and **C.** Quantification of the number of cells (Hoechst) (**B**) and of the percentage of neurons (HuC/D) (**C**) after MKC treatment. **D.** Analysis of spliced *XBP1* (*XBP1s*) expression normalized to total *XBP1* (*XBP1t*) in WS5 neurons treated with 2.5 µM MKC or control DMSO. **E.** Phase contrast images of WS5 neurons at DIV 18 treated or not with 10 µM salubrinal or control DMSO. Scale bars, 200 µm. **F.** and **G.** Quantification of the number of cells (Hoechst) (**F**) and of the percentage of neurons (HuC/D) (**G**) after salubrinal treatment. **H.** Phase contrast images of WS5 neurons at DIV 18 treated or not with 10 µM ceapin-A7 or control DMSO. Scale bars, 200 µm. **I.** and **J.** Quantification of the number of cells (Hoechst) (**I**) and of the percentage of neurons (HuC/D) (**J**) after ceapin-A7 treatment. For all analyses, data are presented as mean ± SEM (n = 3 biologically independent differentiations; **p < 0.01; one-way ANOVA with Dunnett's post hoc test).

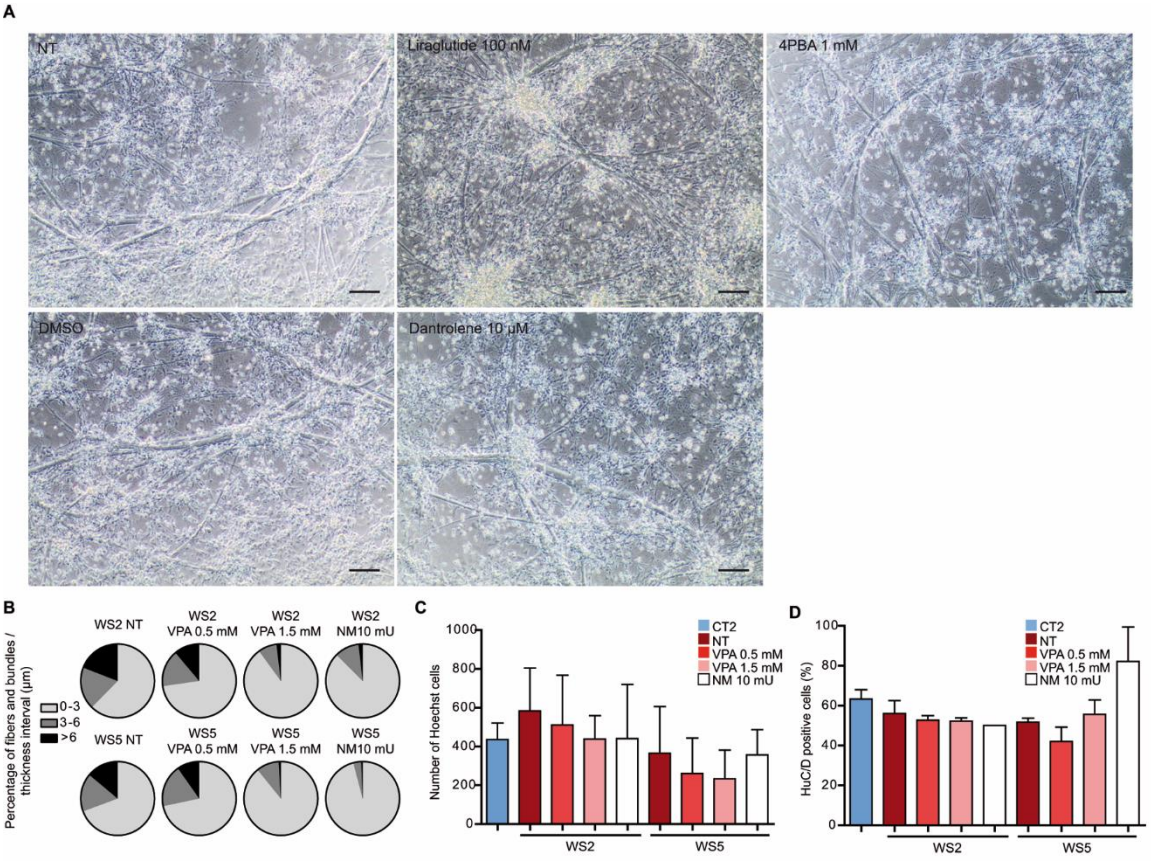

Figure S6: Effect of drugs treatments on the neurite outgrowth defect in WS5 neurons. A. Phase contrast images of WS5 neurons at DIV 18 treated or not (NT) with 10 µM dantrolene, 100 nM liraglutide or 1 mM 4-phenylbutyric acid (4PBA). Scale bars, 200 µm. **B.** Repartition profile of the percentage of isolated and bundled neurites per thickness intervals after VPA treatments. **C.** and **D.** Quantification of the number of cells (Hoechst) (**C**) and of the percentage of neurons (HuC/D) (**D**) after VPA treatments. Data are presented as mean ± SEM (n = 3 biologically independent differentiations; *p<0.05; No statistical difference was observed using one-way ANOVA with Dunnett's post hoc test, data are compared to CT2 cells).

Table S1: Information on iPS cell lines.

iPSC lines	Source of iPSC	Mutations in *WFS1* gene	Sex	Clinical features
WS1	New York Stem Cell Foundation	c.1230-1233delCTCT [p.Val412fs*440]; c.2171C>T [p.Pro724Leu]	Male	Diabetes mellitus; optic atrophy; cognitive disabilities
WS2	New York Stem Cell Foundation	c.1230-1233delCTCT [p.Val412fs*440]	Female	Diabetes mellitus; optic atrophy; cognitive disabilities; diabetes insipidus
WS5	I-Stem	c.1060-1062delTTC [p.Phe354del]; c.1676C>A [p.Ala559Asp]	Female	Diabetes mellitus; optic atrophy
CT1	I-Stem	None	Male	N/A
CT2	I-Stem	None	Female	N/A
CT3	I-Stem	None	Female	N/A

Table S2: List of antibodies, hosts, providers and dilutions.

Application	Antibody	Host	Provider	Dilution
Immunostaining	OCT4	Rabbit	Cell Signaling Technology	1/200
	TRA-1-60	Mouse	Cell Signaling Technology	1/1000
	NANOG	Rabbit	Cell Signaling Technology	1/800
	SSEA4	Mouse	Cell Signaling Technology	1/500
	TUJ1 (neuron-specific class III beta-tubulin)	Chicken	Millipore	1/1000
	SOX17	Goat	R&D systems	1/200
	SMA	Mouse	Agilent Dako	1/100
	AFP	Mouse	Cell Signaling Technology	1/100
	NESTIN	Rabbit	Millipore	1/500
	Ki67	Mouse	Agilent Dako	1/500
	HuC/D (Elav family members HuC, HuD)	Mouse	ThermoFisher Scientific	1/250
	CUX2 (Cut-Like Homeobox 2)	Rabbit	Abcam	1/500
	Alexa Fluor™ 555 Donkey anti-rabbit	Donkey	ThermoFisher Scientific	1/1000
	Alexa Fluor™ 555 Goat anti-chicken	Goat	ThermoFisher Scientific	1/1000
	Alexa Fluor™ 555 Goat anti-mouse	Goat	ThermoFisher Scientific	1/1000
	Alexa Fluor™ 488 Chiken anti-rabbit	Chicken	ThermoFisher Scientific	1/1000
	Alexa Fluor™ 488 Goat anti-mouse	Goat	ThermoFisher Scientific	1/1000
Western-Blot	WOLFRAMIN	Rabbit	Cell Signaling Technology	1/500
	β-ACTIN	Mouse	Li-Cor Biosciences	1/5000
	IRDye 800CW Donkey anti-rabbit	Donkey	Li-Cor Biosciences	1/10000
	IRDye 800CW Donkey anti-mouse	Donkey	Li-Cor Biosciences	1/10000

Table S3: List of primers used for PCR and qPCR.

Gene	Primer	5'-3' Sequence
18S	Forward	GAGGATGAGGTGGAACGTGT
	Reverse	TCTTCAGTCGCTCCAGGTCT
XBP1	Forward	GAAGCCAAGGGGAATGAAGT
	Reverse	GGGAAGGGCATTTGAAGAAC
UNC5D	Forward	ATACCCCAATGCCAAAGGC
	Reverse	TTCAAAATGACAGCAGATGGGC
SLIT3	Forward	GCGATTTGGAGATCCTTACCCT
	Reverse	AGTCGCAGTACAGGTGGTTG
TNC	Forward	TCTGATGGGGGTGGATGGAT
	Reverse	CTTCTCTGCGGTCCCCAAAT
EPHB1	Forward	TCTTCGAGCCCAACCAGAAC
	Reverse	TCTGTGTAGATGCGATGGGC
SEMA4A	Forward	CTTGGTGGATGGGATGCTCTA
	Reverse	GGAGGAAGTTGTCGGTCTTG